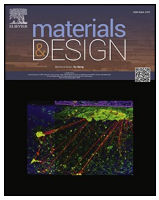
Materials & Design 260 (2025) 115247



Contents lists available at ScienceDirect

Materials & Design

journal homepage: www.elsevier.com/locate/matdes



Inter-pass peening for residual stress control in additive manufacturing: validation using ultrasonic, X-ray and contour method

Joseph Walker [a,*], Brandon Mills [a], Yashar Javadi [a,b], Charles MacLeod [a], Yongle Sun [c], Bilal Ahmad [d], Stewart Williams [c], Jialuo Ding [c], Saeed Tamimi [b,e,f]

[a] Centre for Ultrasonic Engineering (CUE), Department of Electronic & Electrical Engineering (EEE), University of Strathclyde, Glasgow G1 1XQ, UK
[b] Department of Design, Manufacturing & Engineering Management (DMEM), University of Strathclyde, Glasgow G1 1XQ, UK
[c] Welding and Additive Manufacturing Centre, Cranfield University, Milton Keynes MK43 0AL, UK
[d] Centre for Manufacturing and Materials, College of Engineering, Environment and Science, Coventry University, Coventry CV1 5FB, UK
[e] Advanced Forming Research Centre (AFRC), University of Strathclyde, Glasgow PA4 9LJ, UK
[f] National Manufacturing Institute Scotland (NMIS), University of Strathclyde, Glasgow PA3 2EF, UK

ARTICLE INFO

Keywords:
RS measurement
Phased array ultrasonic testing
Wire-arc additive manufacturing
Contour method (CM)
X-ray diffraction (XRD)
Inter-pass peening

ABSTRACT

In this study, round-robin experiments were carried out to evaluate the effectiveness of inter-pass peening as an in-process residual stress (RS) mitigation technique for Wire Arc Additive Manufacturing (WAAM) of Ti-6Al-4V components. A newly developed method, Phased Array Ultrasonics for Residual Stress Measurement (PAURS), was evaluated for its capability to accurately characterise residual stress distributions. To validate PAURS, two established techniques, X-ray Diffraction (XRD), a non-destructive method, and the Contour Method (CM), a destructive technique, were employed. PAURS, particularly when implemented with Full Matrix Capture (FMC), demonstrated enhanced accuracy through improved data redundancy and outlier rejection. Results from PAURS and XRD showed good qualitative agreement with finite element (FE) models derived from CM data, despite some quantitative differences. Inter-pass peening was found to significantly reduce tensile RS in the heat-affected zone, with performance comparable to post-process peening. These findings support the use of inter-pass peening as an effective in-process RS mitigation strategy and highlight the potential of PAURS as a reliable, non-destructive RS measurement method for WAAM Ti-6Al-4V components.

1. Introduction

Additive manufacturing (AM) has gained significant popularity in high-performance industries such as aerospace and automotive, particularly for producing complex, large-scale metallic components. Among AM techniques, Wire Arc Additive Manufacturing (WAAM) has become a practical method for producing large titanium components due to its high build rates and efficient material usage [1]. Specifically, titanium alloy Ti-6Al-4V is a common material choice for WAAM because of its high strength-to-density ratio and corrosion resistance [2].

However, repeated thermal cycling during the layered construction generates significant tensile residual stresses (RS) that can lead to distortion, cracking, and reduced fatigue performance. Therefore, reliable measurement and in-process mitigation of RS are crucial for the viability of WAAM components [3]. One promising approach is peening, which can be implemented either after the WAAM is ended, called post-peening, or during the WAAM process, called inter-pass peening. This technique aims to redistribute and reduce harmful tensile RS by inducing beneficial compressive stresses [4].

While inter-pass peening has shown potential in improving mechanical properties [5], its specific impact on RS distribution in WAAM Ti-6Al-4V components remains underexplored. Accurate RS measurement is essential to validate the effectiveness of such mitigation methods. Traditional techniques like the Contour Method (CM) [6] and X-ray Diffraction (XRD) [7] are well-established for RS evaluation, offering destructive and non-destructive measurements, respectively.

However, there is growing interest in developing non-destructive, in-process-capable approaches that can provide reliable RS measurements

* Corresponding author.
E-mail addresses: j.walker@strath.ac.uk (J. Walker), brandon.mills@strath.ac.uk (B. Mills), yashar.javadi@strath.ac.uk (Y. Javadi), charles.macleod@strath.ac.uk (C. MacLeod), yongle.sun@cranfield.ac.uk (Y. Sun), ac2333@coventry.ac.uk (B. Ahmad), s.williams@cranfield.ac.uk (S. Williams), jialuo.ding@cranfield.ac.uk (J. Ding), saeed.tamimi@strath.ac.uk (S. Tamimi).

https://doi.org/10.1016/j.matdes.2025.115247
Received 18 September 2025; Received in revised form 26 November 2025; Accepted 28 November 2025
Available online 30 November 2025
0264-1275/© 2025 The Authors. Published by Elsevier Ltd. This is an open access article under the CC BY license (http://creativecommons.org/licenses/by/4.0/).

with minimal disruption to the manufacturing workflow [8]. This study evaluates a newly developed technique: Phased Array Ultrasonics for Residual Stress Measurement (PAURS). Javadi et al [9] carried out an initial feasibility study to measure RS in WAAM samples; however, final RS measurements were not achieved until the setup was further expanded on by Walker et al [10]. PAURS was then introduced by Mills et al [11] in welding components. PAURS utilises Longitudinal Critically Refracted (LCR) waves and Full Matrix Capture (FMC) to enhance measurement accuracy and spatial resolution.

The main aim of this study is to build upon the studies carried out by Javadi et al [9], Walker et al [10], and Mills et al [11], and to assess the feasibility and reliability of PAURS for RS measurement in WAAM Ti-6Al-4V components. To validate PAURS, its results are compared against those obtained from CM and XRD. Three samples were measured: an as-deposited sample, an inter-pass peened sample, and a post-peened sample. This allows for both the evaluation of inter-pass peening as a RS mitigation method and the validation of PAURS as a RS measurement technique. The findings contribute to the goal of enabling in-process RS inspection in metal additive manufacturing.

2. Principles and concepts

2.1. Machine hammer peening (MHP) and inter-pass peening

Machine Hammer Peening (MHP) is a surface treatment that uses a pneumatically or electrically driven oscillating tool to deliver controlled, high-frequency impacts on the material surface. Unlike shot peening, which relies on random media impacts and is unsuitable for in-process WAAM applications, MHP provides precise and repeatable strikes, making it ideal for robotic integration and inter-pass application during additive manufacturing [12]. The process induces beneficial compressive RS, improves surface finish, and promotes microstructural refinement by transforming coarse columnar β grains into finer equiaxed structures [13]. These changes reduce anisotropy and enhance fatigue performance in Ti-6Al-4V components [14]. Studies have shown that MHP applied during WAAM significantly decreases RS and improves mechanical properties [15]. Its ability to be applied in-process without removing the part from the build setup makes MHP a practical and effective RS mitigation strategy for large-scale WAAM components [12,15].

Inter-pass peening is a variation of this technique applied during additive manufacturing, specifically between deposition layers. Unlike conventional post-process peening, inter-pass peening is integrated into the build process, offering the potential to mitigate RS accumulation in real time. The process is particularly relevant for WAAM, where high thermal gradients and repeated heating cycles lead to significant tensile RS [16].

2.2. Residual stress in additive manufacturing

RS is the internal stress retained in a material when external forces or thermal gradients are no longer present [17]. In additive manufacturing, RS arises primarily due to non-uniform thermal expansion and contraction during layer-by-layer deposition [18].

RS spans macroscopic fields that equilibrate over structural length-scales (Type I), micro-scale fields associated with grain-scale heterogeneity (Type II) and crystallographic defects (Type III) [19]. In WAAM, Type I RS is of primary concern due to their macroscopic scale and their ability to distort components, as well as causing cracking and degradation of fatigue performance [20]. While Type II and Type III RS occur at smaller length scales, they remain relevant, particularly in influencing phase stability and producing microcracks.

While Tensile RS is particularly detrimental, compressive RS is often beneficial and intentionally introduced through processes like peening [21].

2.3. Contour method (CM)

CM is a destructive technique for measuring RS by cutting a component and measuring the resulting deformation of the cut surfaces. The deformation profile is then used to reconstruct the original RS distribution via finite element (FE) analysis [22]. This method is based on Bueckner's superposition principle, which relates the stress released by a cut to the original stress field [23].

CM is particularly effective for mapping RS across large cross-sections and has been widely used in AM research [24]. However, due to it being a destructive method, its applicability in manufacturing is limited.

2.4. X-ray diffraction (XRD)

XRD is a non-destructive technique that measures RS by detecting changes in the spacing of crystal lattice planes due to elastic strain [25]. It is most effective for surface and near-surface stress analysis, with penetration depths typically limited to tens of microns. The method relies on Bragg's law to relate diffraction angle shifts to strain, which is then converted to stress using elastic constants.

XRD is widely used for validating other RS measurement methods and is suitable for materials with fine, crystalline microstructures [26].

2.5. Phased array ultrasonics for residual stress measurement (PAURS)

PAURS is a non-destructive ultrasonic technique based on the acoustoelastic effect, where stress influences the velocity and time-of-flight (ToF) of LCR waves [11]. RS is measured by relating ToF variations to stress through the acoustoelastic constant, which incorporates second and third-order elastic constants. The full theoretical framework, including derivations and equations for direct and FMC approaches, was previously discussed by Walker et al [10].

The theoretical framework links wave velocity to strain using Lamé constants (λ, μ) and higher-order terms, leading to the core stress ToF. The acoustoelastic constant (L_{11}) is determined via tensile testing combined with ultrasonic measurements, where incremental loading allows mapping of ToF changes to applied stress. PAURS can then calculate RS using either a direct approach, considering only straight transmitter–receiver paths, or an FMC approach, which accounts for all possible acoustic paths to improve data accuracy.

3. Sample manufacturing

Three Ti-6Al-4V samples were manufactured using the WAAM process to investigate the effects of inter-pass peening on RS distribution. All samples were fabricated with identical geometries of 250 mm × 60 mm × 73 mm and consisted of 10 deposited layers.

The three samples are as follows:

- As-deposited (no peening),
- Inter-pass peened (peening applied during deposition),
- Post-peened (peening applied after deposition).

Figs. 1 and 2 shows a schematic of the WAAM sample manufacturing and the physical setup, respectively. A 1.2 mm diameter Ti-6Al-4V wire was used as the feedstock. Deposition was performed using a Plasma Transferred Arc (PTA) system, with a wire feed speed of 2.2 m/min and a current of 180 A. The travel speed was varied: the first layer was deposited at 4 mm/s, the second at 4.5 mm/s, and the remaining layers at 5 mm/s. The average layer height was approximately 0.98 mm, and the wall width was 9.2 mm.

The three separate samples were measured with three RS measurement methods. The individual samples and the methods used for each of them are shown in Fig. 3. All samples are shown from the bottom surface, which was the primary focus for RS data collection across all

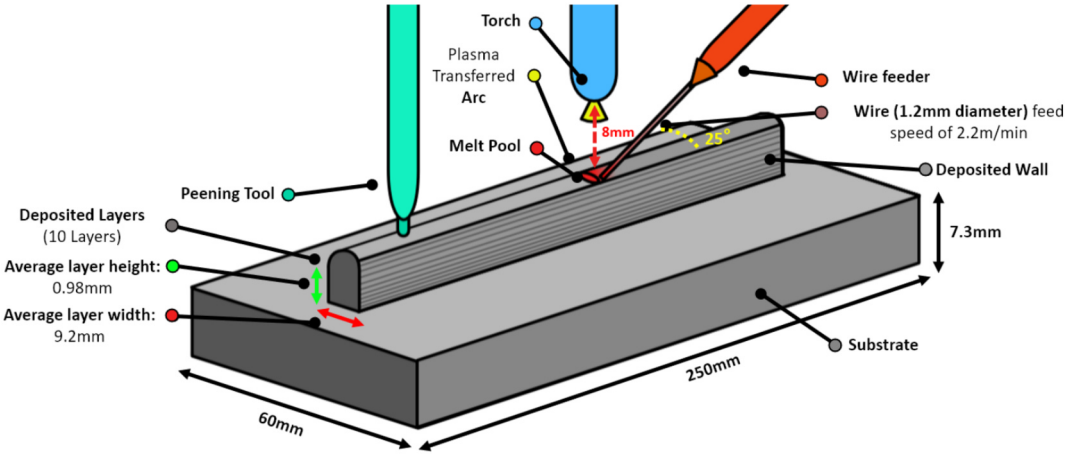


Fig. 1. Schematic of the setup and dimensions for the manufactured experimental samples.

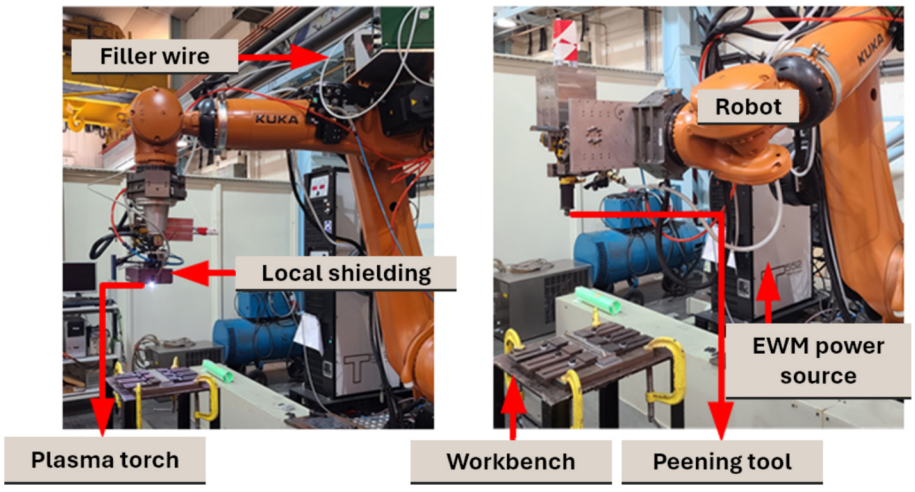


Fig. 2. Physical setup for the manufacturing and peening of the WAAM samples.

methods.

A hammer peening tool (Atlas RRH06P) was integrated into the deposition setup for the inter-pass peened sample. The pneumatic tool was mounted with the robot and provided an energy per blow of 6 J (7 bar air pressure). The peening head had a diameter of 10 mm, operated at a frequency of 36 Hz, and travelled at 10 mm/s.

The substrate was clamped using six evenly spaced clamps to minimise distortion during deposition. Shielding was provided by pure argon gas, with flow rates of 0.8 L/min for the plasma gas, 8 L/min for the shielding gas, and 68 L/min for the local shielding device. All samples were built using a 6-axis KUKA robotic arm, which controlled the deposition path in an alternating travel direction to ensure uniform heat distribution.

4. Methods and procedures

4.1. Measurement methodology

The experimental workflow was divided into three main RS measurement techniques: PAURS, CM, and XRD. Each method was applied to a specific combination of samples to evaluate both the effectiveness of inter-pass peening and the reliability of PAURS as a measurement technique.

- PAURS was applied to the as-deposited and inter-pass peened samples.
- CM was applied to the as-deposited and post-peened samples.
- XRD was applied only to the as-deposited sample for validation purposes.

XRD Procedure:

The as-deposited sample was prepared by cleaning the surface to remove oxides and debris. Measurements were performed using a PROTO LXRD diffractometer, applying the $\sin^2\psi$ method. Fifteen points were measured along the bottom of the sample. Data were processed using XRDWin 2.0 software, and stress values were calculated using material-specific X-ray elastic constants.

CM Procedure:

Two samples (as-deposited and post-peened) were cut using wire electro-discharge machining. The cut surfaces were scanned using a coordinate measuring machine to obtain displacement profiles. These were processed in MATLAB and used to generate FE models in Abaqus to reconstruct the RS fields.

PAURS Procedure:

The PAURS method involved two stages:

1. Determination of the acoustoelastic constant via tensile testing on a Ti-6Al-4V specimen using the same ultrasonic setup.

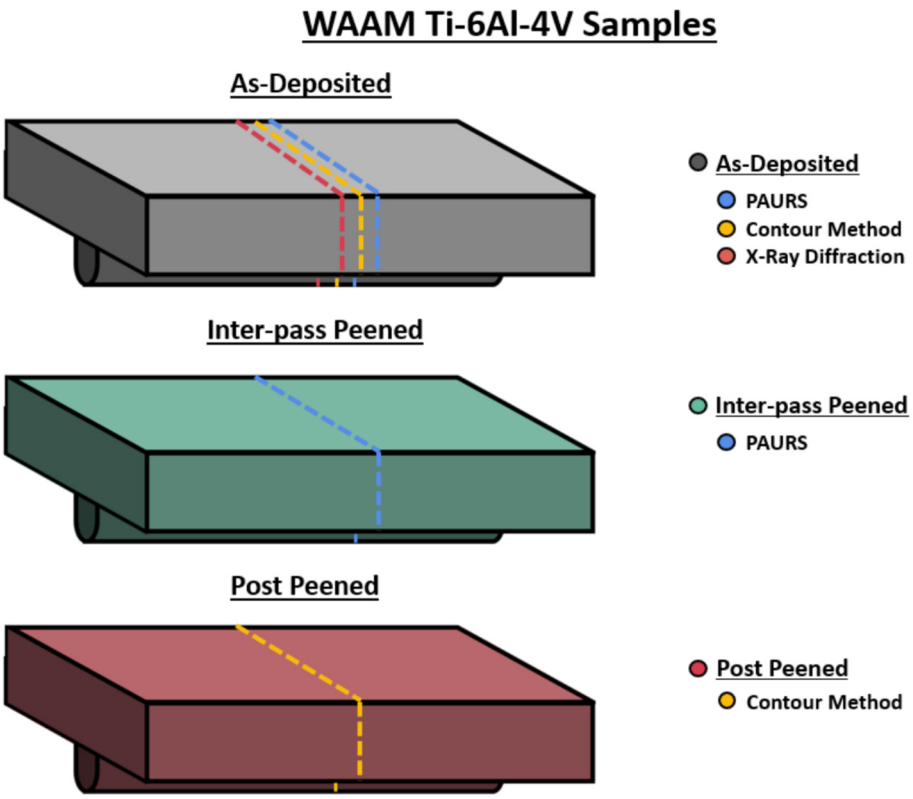


Fig. 3. The RS measurement methods used for each WAAM Ti-6Al-4V sample.

2. ToF measurements along the bottom of both the as-deposited and inter-pass peened samples.

A wedge angle study was conducted to determine the optimal angle for LCR wave generation in Ti-6Al-4V. The final PAURS measurements were processed using the FMC approach, with FMC used to enhance data and allow for outlier removal.

Measurement uncertainties vary across the RS evaluation techniques used in this study. For the CM, uncertainty primarily arises from surface displacement measurement and FE reconstruction, with typical values reported as ± 20–30 MPa for titanium and high-strength alloys [24,27]. For XRD, using the $\sin^2\psi$ method, errors are generally ± 10–20 MPa, influenced by peak fitting and elastic constant accuracy [28,29]. For PAURS, uncertainty depends on ToF resolution and acoustoelastic constant determination; studies on Ti-6Al-4V WAAM components report values of approximately ± 25–40 MPa after FMC averaging and outlier removal [10,11].

4.2. Contour method

CM was used to measure RS in the as-deposited and post-peened samples. Both samples were sectioned vertically using a Fanuc Robocut α-C600i wire electro-discharge machine (EDM) with a 0.25 mm brass wire. The cut was initiated from the top of the deposit and progressed downward through the substrate. Both samples were clamped symmetrically, and low electrical power parameters were used for better surface finish and fewer wire EDM cutting errors at the cut perimeter.

A cutting speed of approximately 0.25 mm/min was used, and displacement profiles of the cut surfaces were measured using a Zeiss Contura g2 coordinate measuring machine with a 3 mm drag probe. Measurement points were spaced at 0.2 mm intervals in both directions from the sample perimeter. The displacement data were processed in MATLAB, including cleaning, alignment, flattening, and smoothing using a cubic spline with 2.5 mm knot spacing in both X and Y directions. FE models of one half of each sample were developed in Abaqus 2021 using eight-node brick elements (C3D8R).

4.3. X-ray diffraction

Fig. 4 illustrates the procedure used for collecting XRD data. As XRD was selected to validate both CM and PAURS as RS measurement methods, measurements were taken along the bottom of the sample for direct comparison. Only the as-deposited sample was analysed, as the purpose was validation rather than comparison with the inter-pass peened condition. Fifteen measurement points were taken along the bottom surface to provide a representative RS distribution for comparison with CM and PAURS results.

Fig. 5 shows the full experimental setup for the XRD measurements on the as-deposited Ti-6Al-4V WAAM sample. RS measurements were performed using a PROTO LXRD diffractometer, applying the $\sin^2\psi$ method, which is widely used for stress analysis in polycrystalline materials. This technique involves tilting the sample at various ψ angles to detect changes in lattice spacing, from which strain and stress are calculated. Due to the limited penetration depth of X-rays (typically a few tens of microns), the method is ideal for surface and near-surface

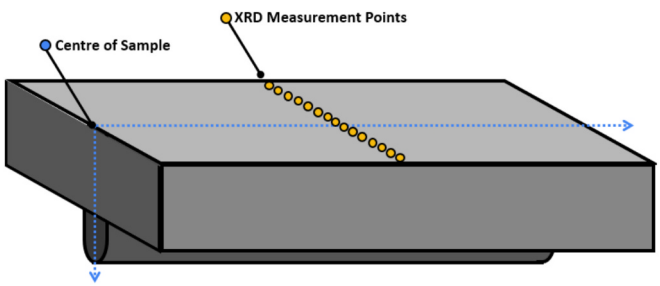


Fig. 4. Method for data collection using XRD.

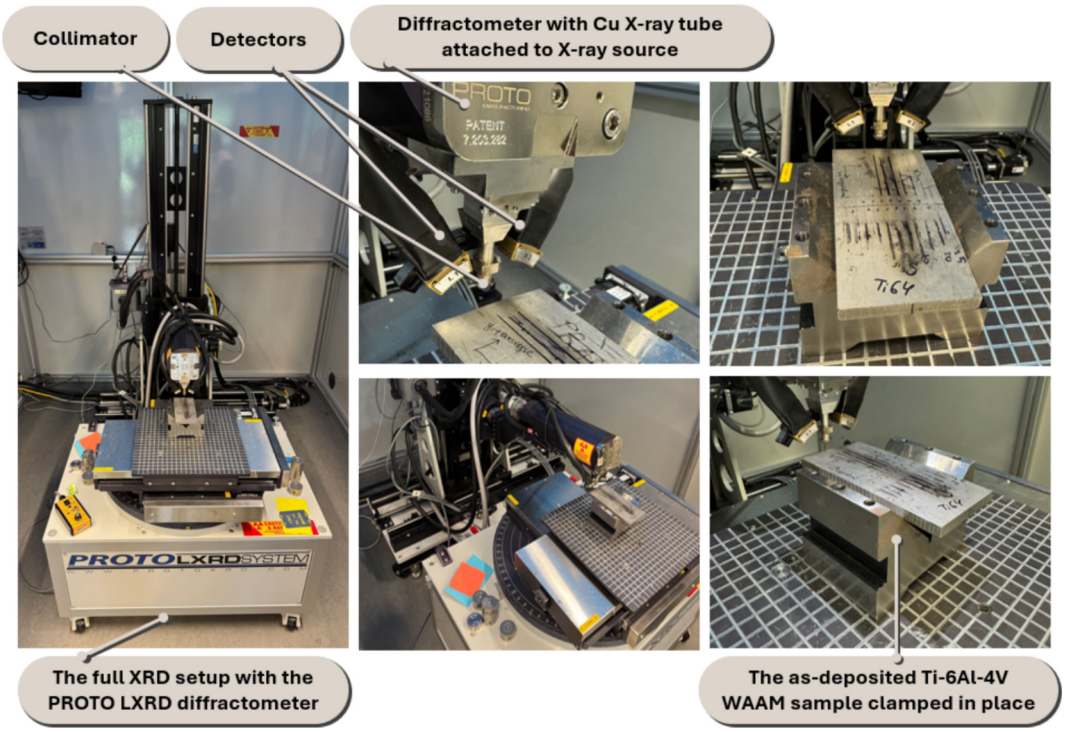


Fig. 5. Full experimental setup for the XRD measurements.

stress evaluation in additively manufactured parts.

Data were processed using PROTO XRDWin 2.0 software. "Longitudinal" and "transverse" refer to directions parallel and perpendicular to the WAAM build path, respectively, to capture directional stress variations. Material-specific X-ray elastic constants (XECs) were sourced from the instrument's internal database. Peak positions were fitted using a 75 % Gaussian function, and peak shifts were determined using the Absolute Peak method to ensure consistent and accurate stress calculations. Table 1 summarises the scan parameters, including tilt angles, exposure times, and the selected diffraction plane.

4.4. Phased array ultrasonic residual stress (PAURS) measurements

4.4.1. Angle/distance study

A novel approach was developed for this study to enhance RS measurements compared to the conventional LCR method using single-element transducers, as previously demonstrated by Walker et al [10]. The PAURS setup consists of two 5 MHz, 8-element ultrasonic phased arrays placed in an acrylic wedge, one as a transmitter, the other as a receiver. This configuration significantly increases the number of LCR wave paths, improving measurement reliability.

Traditional LCR setups generate only two wave paths, limiting their ability to mitigate interference from material texture and microstructure. The PAURS setup, by contrast, can generate at least 8 acoustic paths and up to 64 paths using FMC, increasing the number of acoustic paths and improving measurement accuracy significantly.

The wedge angle is critical for effective ultrasound propagation. Based on Snell's law, several angles were tested to determine the optimal configuration for Ti-6Al-4V. A 22.7° wedge was found to require the least gain for a clear LCR peak.

Table 1
The scan parameters used for XRD RS measurements.

Parameter	
Diffraction plane (h,k,l)	213
Crystal structure	HCP
Tube	Cu Kα
Wavelength, nm	1.541838
Aperture (round), mm	1
Acceleration voltage, kV	30
Current, mA	30
½ S2, MPa^{-1}	$11.89 * 10^{-8}$
−S1, MPa^{-1}	$2.97 * 10^{-8}$
Bragg Angle, deg.	142.0

4.4.2. PAURS experimental setup

Fig. 6 shows the experimental setup used for PAURS ToF measurements, which utilises a PEAK Micropulse 6 phased array instrument in combination with LabVIEW. Scans were carried out along the bottom surfaces of both the as-deposited and inter-pass peened WAAM Ti-6Al-4V samples. To ensure consistent spacing, a ruler was used to guide the scanning process, with measurements taken at 5 mm intervals outside the HAZ and at 1 mm intervals within it.

The important data to collect from the collected ToF measurements is the zero-crossing point. The zero crossing needs to be taken from every signal for the data collected. For example, if using the direct approach, it needs to be taken from each of the 8 signals, but with FMC, this increases to 64, so it will need to be taken from each of the 64 signals. These zero crossing values are then later used alongside the acoustoelastic constant data to produce the RS measurements.

4.4.3. PAURS-ToF consistency

It is important to note that the ToF for LCR waves remains consistent regardless of the LCR path or the number of transmitter and receiver elements. This consistency was demonstrated by Javadi et al in their feasibility study of the PAURS method [30].

Fig. 7 provides geometrical proof showing that ToF remains unchanged whether Element n transmits a wave travelling distance A1 in the wedge and T + B2 in the Ti-6Al-4V sample, or Element m transmits a wave travelling distance A2 in the wedge. This confirms that all elements in the transducer yield the same ToF, regardless of the LCR wave path between transducers.

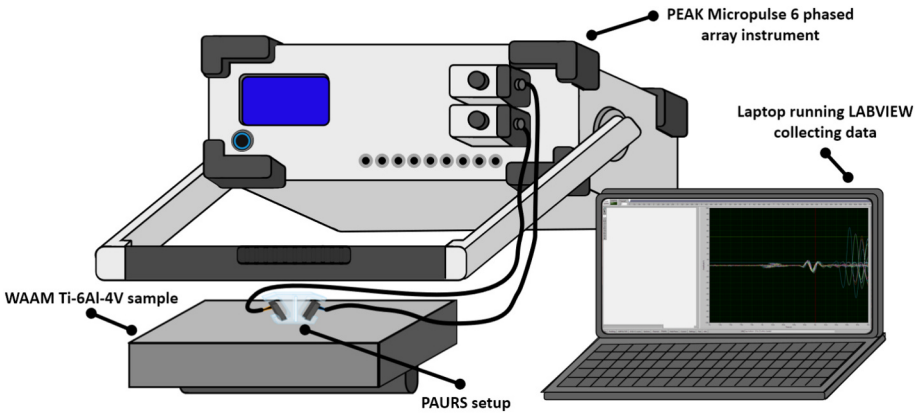


Fig. 6. Experimental setup for PAURS ToF measurements.

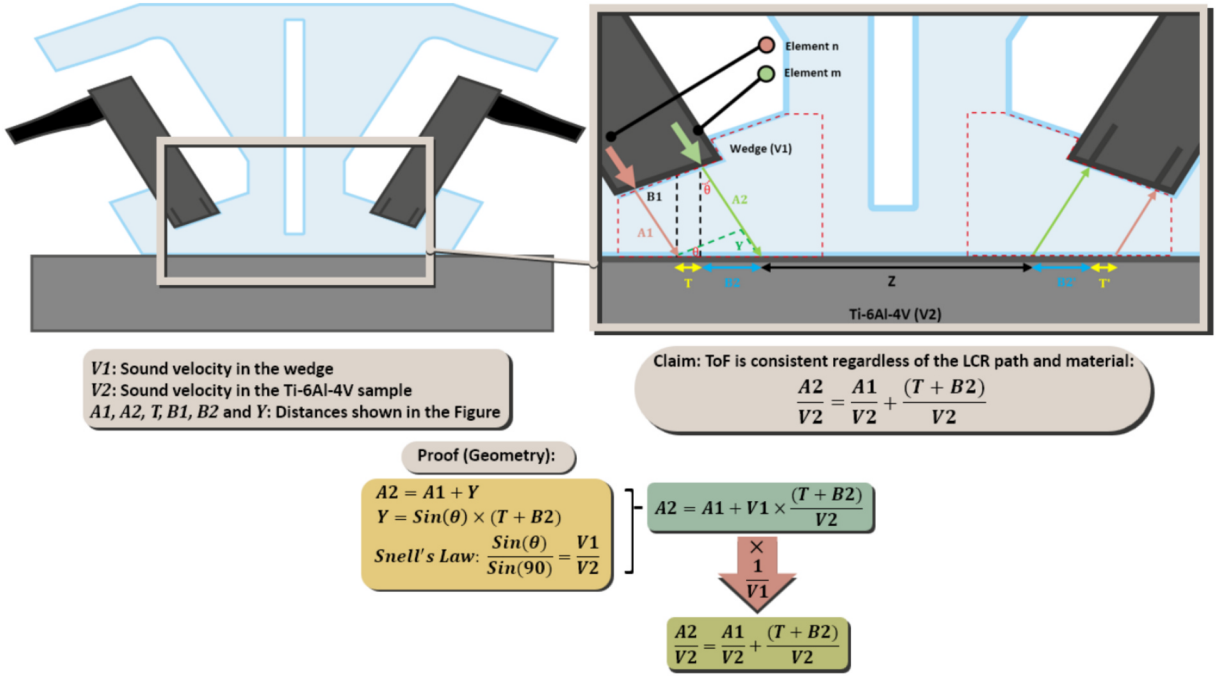


Fig. 7. Geometrical proof of ToF consistency.

4.4.4. LCR wave propagation

It is also crucial to understand that ultrasonic waves do not travel in straight lines. LCR waves exhibit specific beam profiles upon refraction in the sample. Fig. 8 (a) illustrates how a single element generates an LCR wave, showing its beam profile and refraction angles. The principal lobe, containing most of the energy, refracts at 84°, while a stronger side lobe appears at 67° [31].

Fig. 8 (a) Single element LCR beam profile in a WAAM sample (b) 4-element phased array LCR beam profile. (b) illustrates an example of how a 4-element phased array transmitter generates an LCR beam profile as it propagates through the sample. At first glance, the overlapping wavefronts may suggest potential interference or signal crosstalk between elements. However, this is effectively managed in two ways: spatially, by maintaining appropriate spacing (element pitch) between the array elements, and temporally, through the use of delay laws that control the timing of each transmitted signal. These measures ensure that the main LCR waves remain well-defined and travel toward the receiving elements without significant interference, preserving the integrity of the received signals. It is important to note that these assumptions are supported by experimental results presented in this paper. LCR waves exhibit distinct characteristics, such as the fastest wave arriving at the receiver confirming their near-surface propagation, as observed by Mills et al [11] and Walker et al [10], which help distinguish them from other wave modes or noise caused by interference.

While Fig. 8 shows a more realistic depiction of LCR paths, capturing the spread and shape of the ultrasonic energy lobes as they propagate through the material, Fig. 9 simplifies this by representing each path as a straight line. It illustrates how each of the 8 transmitter elements sends LCR waves to all 8 receiver elements, resulting in 64 unique transmit-receive combinations, compared to just 2 in a traditional single-element setup.

Although the straight-line paths in Fig. 9 do not reflect the actual wavefront shapes or energy distribution shown in Fig. 8, they help clarify the FMC process. This schematic highlights how each receiver element captures individual LCR waves from each transmitter, making the inspection coverage and data acquisition strategy easier to interpret. This simplified line representation will be used throughout this paper to discuss the PAURS results.

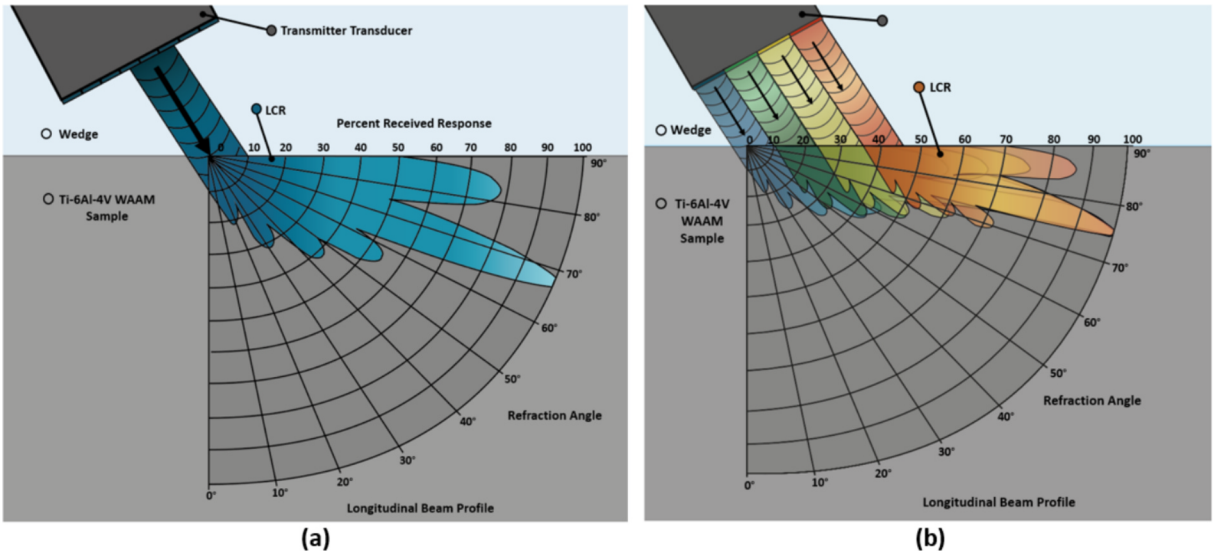


Fig. 8. (a) Single element LCR beam profile in a WAAM sample (b) 4-element phased array LCR beam profile.

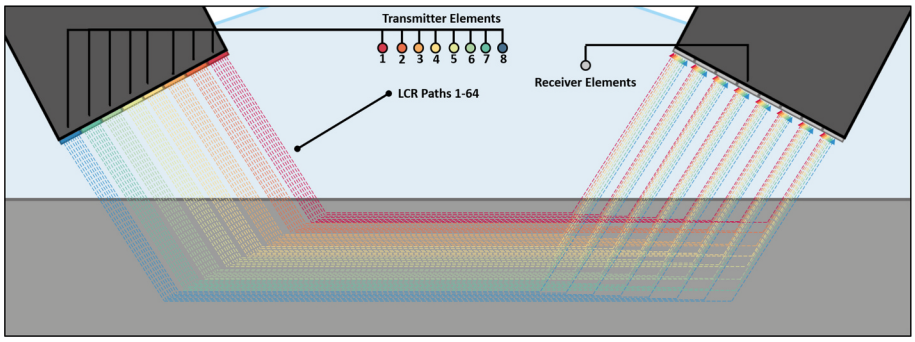


Fig. 9. Schematic of LCR paths using PAURS with two 8-element transducers.

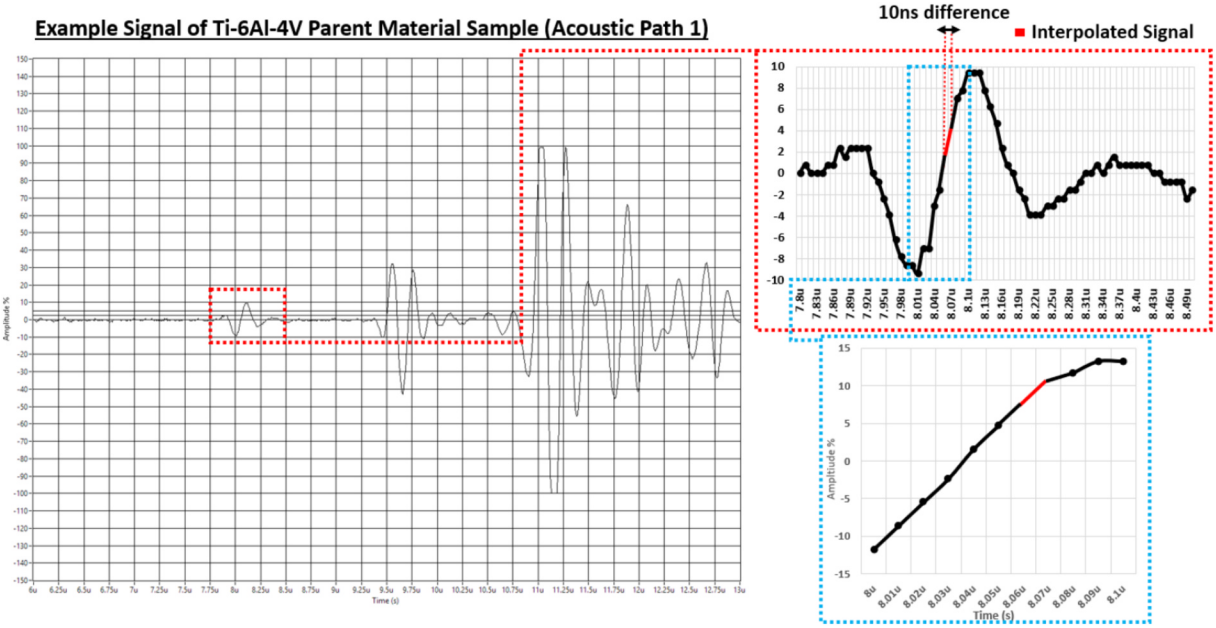


Fig. 10. Example LCR signal showing interpolation in Ti-6Al-4V.

4.4.5. Interpolation

A key advantage of the PAURS method is its ability to address limitations in sampling rate. A key advantage of the PAURS method is its ability to overcome the limitations imposed by conventional ultrasonic sampling rates, which typically restrict time resolution to around 10 to 20 ns. This resolution is insufficient for accurately identifying the zero-crossing point of LCR signals for reliable RS calculations. PAURS addresses this challenge by utilising FMC and interpolation across multiple acoustic paths and reducing timing errors, without the need for expensive high-speed analogue-to-digital converter (ADC) hardware.

Standard ultrasonic equipment typically samples at rates up to 100 MHz, which corresponds to a time resolution of 10 ns or more. However, RS measurements often require much finer resolution, around 1 ns, to accurately determine the zero-crossing point of the LCR signal. To overcome this, interpolation is used to estimate values between sampled points. Javadi et al. demonstrated this approach using synchronised 100 MHz equipment to achieve precise ToF measurements in austenitic stainless steel. [32].

Fig. 10 shows an example of an interpolated LCR signal, where there is a 10 ns gap (using a 100 MHz sample rate) between two sampled points (from 8.05 μs to 8.06 μs). A 100 MHz sampling rate was selected as a practical compromise between hardware capability, data size, and cost. In single-element transducer setups, interpolation is based on only two points, which can introduce significant error, up to 10 ns in this case, when estimating the zero-crossing. While this may be acceptable for general defect detection, it can significantly affect the accuracy of RS measurements.

The PAURS method, using FMC, generates 64 independent LCR signals. This allows interpolation to be performed 64 times, once for each acoustic path, and the results can then be averaged to reduce random error. Fig. 11 presents 8 of these 64 interpolated signals, with zero-crossing times of 8.04, 8.03, 8.035, 8.03, 8.02, 8.01, 8.01, and 8.01 μs for paths 8, 16, 24, 32, 40, 48, 56, and 64, respectively. When all 64 paths are averaged, the resulting interpolated zero-crossing time is 8.023 μs. This averaging process smooths out individual interpolation errors and improves the precision of the ToF measurement. Since the theoretical ToF is identical across all paths, the averaged value provides a more accurate and reliable estimate, something that would be difficult to achieve with a single-element setup.

4.4.6. Scanning

To perform ultrasonic ToF RS measurements effectively, the sample was divided into multiple scan lines, as shown in Fig. 12. The centre of the sample wall is defined as 0 mm, with scan lines extending to ± 25 mm. Because RS is expected to peak within the HAZ due to thermal cycling, that region was scanned more extensively.

Outside the HAZ, 8 measurements were taken at 5 mm intervals: −25, −20, −15, −10 mm on one side, and 10, 15, 20, 25 mm on the other. Within the HAZ, 18 measurements were taken at 1 mm intervals from −9 mm to 9 mm. This increased sampling improves RS resolution in the HAZ.

4.4.7. Correction of couplant thickness effects in ToF measurements

To further improve the reliability of the results, the thickness of the couplant and its effect on the RS measurements had to be considered. Since the ToF measurements were taken along scan lines across the bottom surfaces of both samples, variations in couplant thickness along these lines could impact measurement accuracy. This is illustrated in Fig. 13(a), which shows measurements taken on both the parent material and a WAAM sample. Each of these measurements may be influenced by differing couplant thicknesses, potentially affecting the comparability of results between the two regions. To address this, five separate formulae are presented to demonstrate the process used to eliminate the influence of couplant thickness.

The ToF measured in the parent material (ToF_1) differs from that in the WAAM sample (ToF_2). This difference can be used to measure RS, under the assumption that the only contributing factor to the variation is stress-induced changes in acoustic velocity. However, the total ToF comprises two components:

- ToF_C: Time-of-flight through the couplant layer
- ToF_M: Time-of-flight through the material

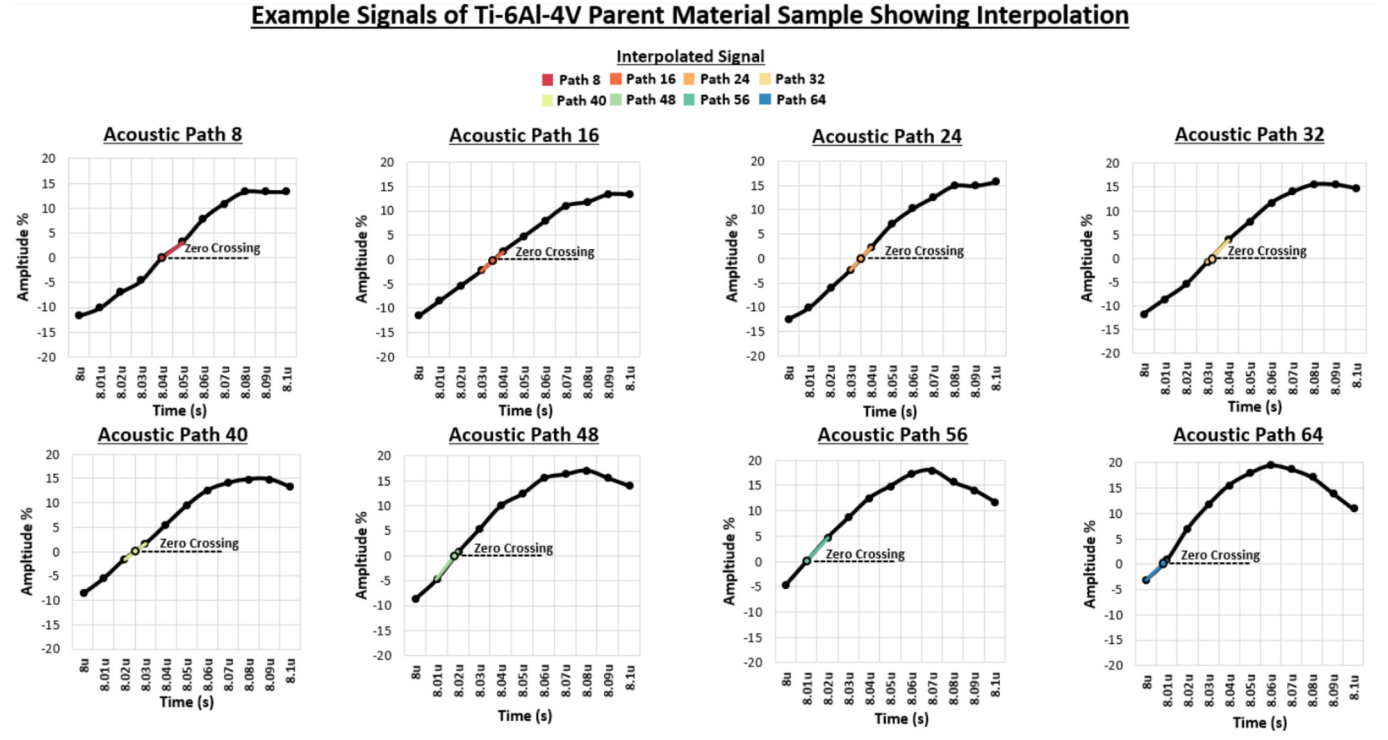


Fig. 11. 8 example interpolated signals from Ti-6Al-4V.

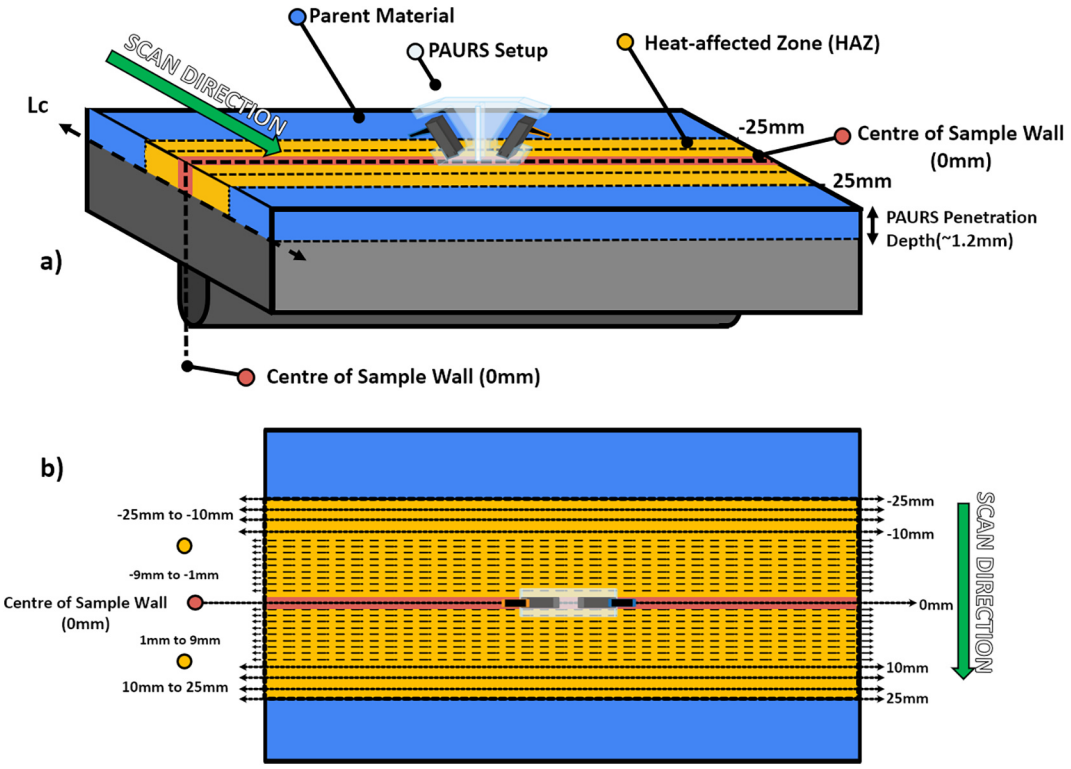


Fig. 12. (a) Schematic of WAAM Ti-6Al-4V scanning; (b) Top-down view of scan lines.

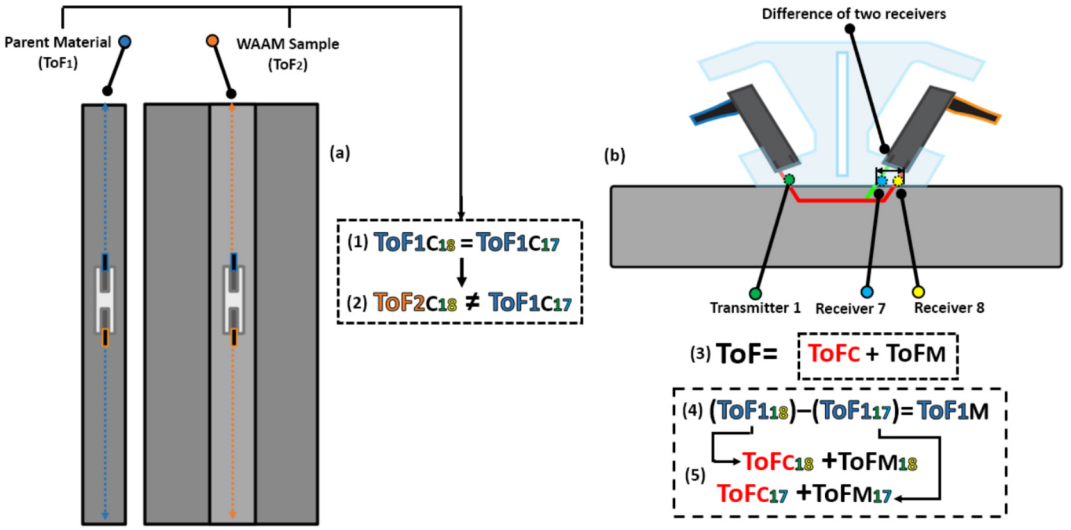


Fig. 13. (a) Couplant thickness variation; (b) Schematic of mitigation using receiver differences.

This relationship is expressed as:

$$ToF = ToF_C + ToF_M \quad (1)$$

Equation 1 Formula to show how the true ToF can be attained by removing the ToF of the couplant

While ToF_M may reflect RS and possibly material texture, which is not addressed in this section, ToF_C can vary due to inconsistencies in couplant thickness, particularly in manual measurements. Therefore, part of the observed difference between ToF_2 and ToF_1 may be attributed to couplant variation rather than material properties.

A traditional approach to mitigate this issue in traditional single-element transducer setups involves using two receivers. Instead of measuring ToF between a transmitter and a single receiver, the difference in ToF between two receivers is calculated (e.g., ToF_{11}-ToF_{12}). Since both paths include the same couplant layer and the wedge remains stationary, the couplant contribution cancels out. The resulting differential measurement isolates ToF_M, which can then be used to calculate the difference between ToF_2 and ToF_1 without the effects of the couplant.

This methodology is further enhanced through the use of the PAURS system. In this configuration, an array of 8 transmitters and 8 receivers enables 64 unique acoustic paths. By applying the same differential approach across multiple transmitter–receiver combinations, the couplant effect can be removed with significantly greater certainty. The redundancy and spatial resolution provided by the array improve the reliability of the correction and improves the RS measurements.

To illustrate this process, Fig. 13 presents a specific example using transmitter element 1 and receiver elements 7 and 8. As shown in Equation 2, the ToF measured in the parent material between transmitter 1 and receiver 8 (ToF_1C_{18}) is equal to that between transmitter 1 and receiver 7 (ToF_1C_{17}), assuming uniform couplant conditions.

$$ToF_1C_{18} = ToF_1C_{17} \tag{2}$$

Equation 2 Formula to represent how the ToF between different receivers is equal in the same material

However, when the same measurement is performed in the WAAM sample (Equation 3), the ToF differs due to changes in material properties and potentially couplant thickness.

$$ToF_2C_{18} \neq ToF_1C_{17} \tag{3}$$

Equation 3 Formula to represent how the ToF is altered at differing scan lines due to the couplant thickness effect

By subtracting the two receiver measurements (Equation 4), the couplant effect is eliminated, isolating the material ToF ($ToF1_M$). This logic is extended across the full array to systematically remove couplant effects from all measurements.

$$\left(ToF_{1_{18}}\right) - \left(ToF_{1_{17}}\right) = ToF_1M \tag{4}$$

Equation 4 Formula to show how the difference between receiver 7 and 8 with transmitter 1 can be used to remove the couplant thickness effect

4.4.8. Acoustoelastic constant

To obtain the acoustoelastic constant required for interpreting the ToF data from the WAAM Ti-6Al-4V samples, tensile testing was performed on a separate Ti-6Al-4V sample.

The acoustoelastic constant is essential for calculating RS, as it defines how ultrasonic wave velocity changes with applied stress, which effectively calibrates PAURS for accurate RS measurement on WAAM samples. Since this relationship is material-specific, testing must be conducted on the same material being evaluated, in this case Ti-6Al-4V, to match the Ti-6Al-4V samples.

Fig. 14 presents a close-up of the acoustoelastic testing setup, which mirrors the configuration used for the ToF measurements. The PAURS system, previously shown in Fig. 8, is used identically here and clamped directly onto the sample to collect measurements at each loading interval.

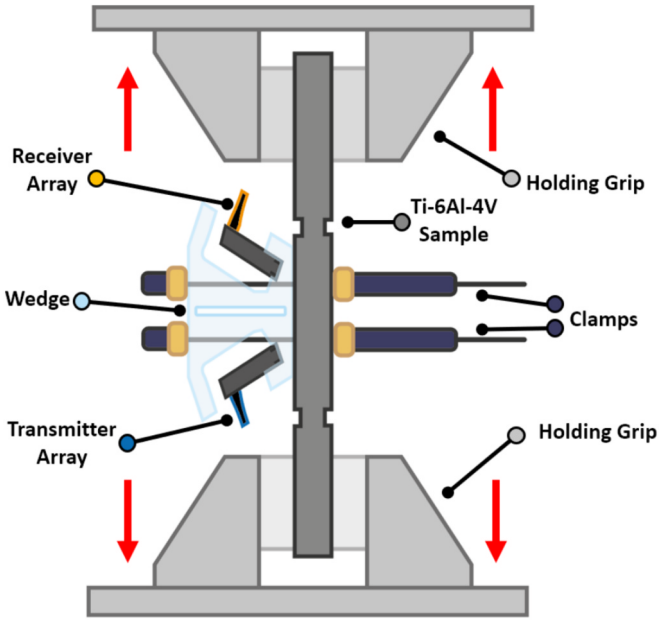


Fig. 14. Close-up of the acoustoelastic constant testing setup.

Similar to the ToF measurements, a PEAK MP6 system connected to a laptop running LabVIEW was used to collect the data. Initial testing was conducted to verify system functionality, applying load increments of 10 kN up to 240 kN, followed by unloading back to 0 kN. Once confirmed, the main test was performed using smaller 2 kN increments up to 250 kN, then unloaded to 0 kN. This procedure enabled analysis of how ultrasonic wave propagation through the material varied with applied stress.

Although a maximum stress of 578.7 MPa could be achieved with 250 kN, a maximum load of 200 kN was ultimately selected. This decision was based on the slotted section of the sample being only 7 mm thick, and because 200 kN was sufficient to gather the necessary data for determining the acoustoelastic constant. During tensile testing, the machine paused at each load interval for 10 s to allow the PEAK MP6 to collect A-scan data.

Two eight-element phased array transducers were used, resulting in 16 data points per load step for both loading and unloading. Each data point was acquired using FMC, producing 64 acoustic paths from the 8 × 8 transducer matrix. Due to the large volume of data generated, the results were averaged to obtain a reliable value for the acoustoelastic constant.

5. Results and discussion

5.1. Microstructure study

5.1.1. Material preparation

Although the focus of this paper is RS rather than microstructure engineering, ultrasonic interpretation is influenced by grain morphology, texture, and α/β distribution. Extensive literature has shown that elongated or textured microstructures increase ultrasonic scattering and attenuation, while equiaxed regions exhibit weaker backscatter and lower frequency-dependent loss [33–37]. To confirm that the WAAM-built Ti-6Al-4V wall used in this study exhibits a representative microstructure, a cross-section was prepared and examined under an optical microscope. A transverse section of the WAAM-built Ti-6Al-4V wall and substrate was prepared for optical microscopy. The sample was cut perpendicular to the build direction using EDM to avoid introducing cutting damage, as shown in Fig. 15 a) and Fig. 15 b) presents montaged optical macrographs of the deposited wall and the substrate.

The mounted specimen was ground sequentially with P240, P400, P800, P1200, and P2500 SiC papers, followed by final polishing on a microcloth using 0.02 μm colloidal silica to achieve a scratch-free finish. The polished surface was etched in Kroll's reagent (ASTM E407 No. 187) by immersion for 10–20 s, rinsed, and dried to reveal the microstructure features.

No apparent macroscopic porosity was observed in the etched section. At the substrate–wall interface, the prior-β grains were largely equiaxed, sizing approximately 0.5 ± 0.3 mm at the base and increasing to roughly 3 ± 1 mm within the first few millimetres of build height, reflecting the accumulation of thermal energy during deposition. Further up the wall, the structure transitioned to columnar prior-β grains oriented along the build direction, extending across several layers and frequently exceeding 3 mm in length until the point where deposition was interrupted. In the HAZ, close to the fusion boundary, a slight increase in grain size relative to the bulk substrate was visible, suggesting local exposure to temperatures near or above the β-transus during deposition. This observation is in line with prior reports for WAAM-processed Ti-6Al-4V [38,39].

It is also worth highlighting that the LCR ultrasonic technique used here penetrates approximately 1–1.2 mm from the bottom surface of the substrate, as indicated by the dashed line in Fig. 15 b). This depth lies well below the heat-affected zone and therefore remains unaffected by the thermal cycles associated with WAAM deposition. As a result, the

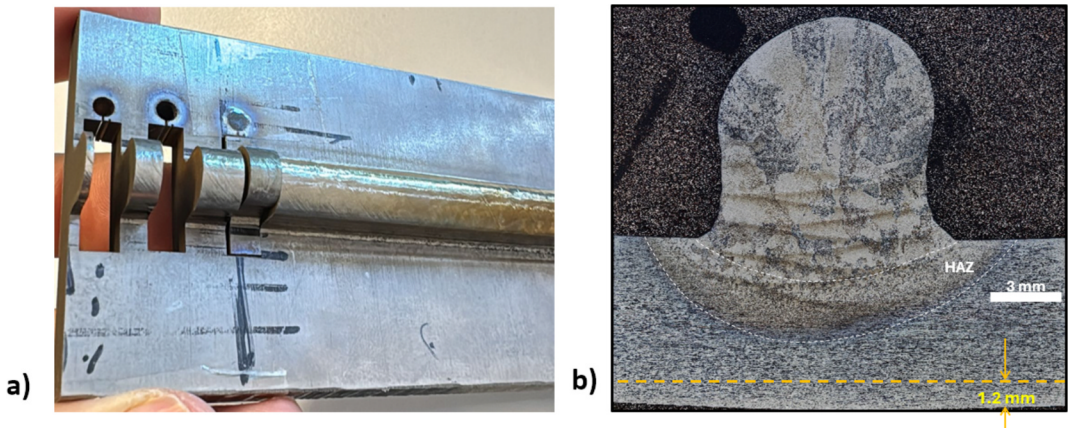


Fig. 15. a) The cut section of the WAAM Ti-6Al-4V wall used for optical microscopy and b) Montaged optical macrographs of the deposited wall and the substrate.

region interrogated during LCR measurements retains a uniform microstructure across the width of the examined section.

5.2. Contour method

Fig. 16 shows the CM RS results for both the as-deposited and post-peened WAAM Ti-6Al-4V samples, alongside a schematic indicating the expected zones within the WAAM samples, aligned with the measurement results.

In the as-deposited sample, RS begins at a minimum of ~ -150 MPa at −35 mm, and increases steadily toward the centre, peaking at ~ 410 MPa at 0 mm, which aligns with the sample wall's centre, where RS is typically highest. Beyond this point, RS remains relatively constant until 9 mm, after which it gradually decreases to ~ -90 MPa at −30 mm, before slightly rising again to ~ 100 MPa after 25 mm.

In the post-peened sample, a clear reduction in the overall RS is examined. While the general trend remains similar with lower RS values further from the centre, there is still a noticeable increase in RS between −10 mm and 10 mm, closely mirroring the peak observed in the as-deposited condition. However, the magnitude of this peak is significantly reduced, with a maximum RS of ~ 130 MPa at 3 mm. Notably, the RS values further from the centre are higher in the post-peened sample compared to the as-deposited one. For instance, at 25 mm, the RS is ~ -200 MPa in the as-deposited sample, whereas it is ~ 0 MPa in the post-peened sample. Similarly, at 30 mm, the RS is about −125 MPa in the as-deposited condition and only −10 MPa after peening. This is expected, as peening does not eliminate RS but rather redistributes it, reducing tensile stress and introducing beneficial compressive stresses to enhance the structural integrity of the sample.

Several anomalies are observed in the CM RS measurements. At the furthest end of the sample at 35 mm, there is a small spike in RS from approximately −200 MPa to −150 MPa, which then returns to −200 MPa. A similar pattern of sharp fluctuations is seen between 17 and 20 mm, where the stress increases and decreases abruptly.

Additionally, the RS distribution is not perfectly symmetrical. This asymmetry is expected due to slight distortions at the bottom of the WAAM Ti-6Al-4V samples, which are not completely flat. This is more clearly illustrated in the CM FE model shown in Fig. 17. Such distortion is a result of stress on the samples during the manufacturing process, which is then relieved, and can potentially influence the measured RS. To minimise this effect, all samples were flat before deposition, and symmetrical clamping was applied using six clamps, with three evenly

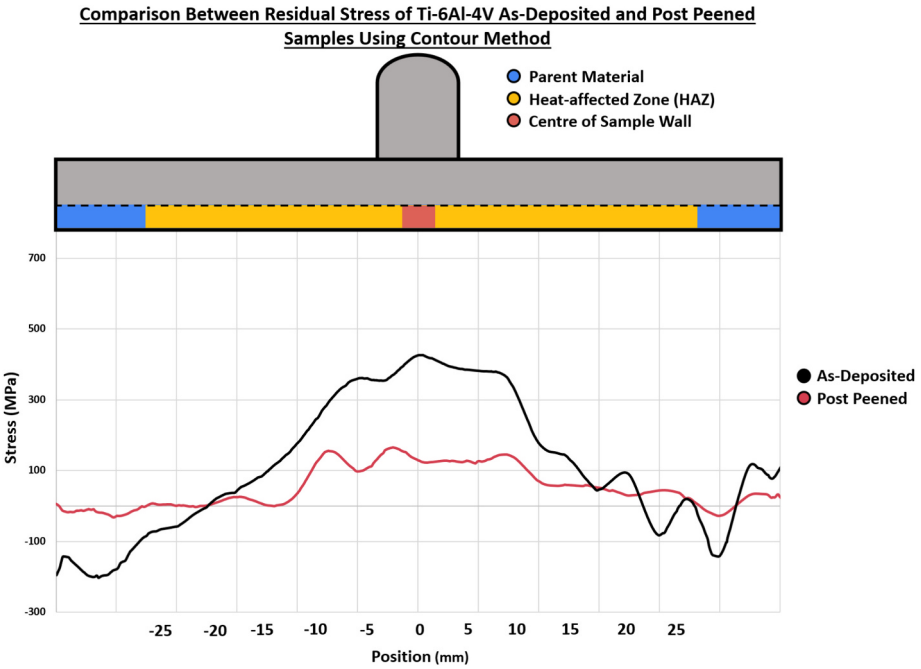


Fig. 16. CM RS measurements for as-deposited and post-peened samples.

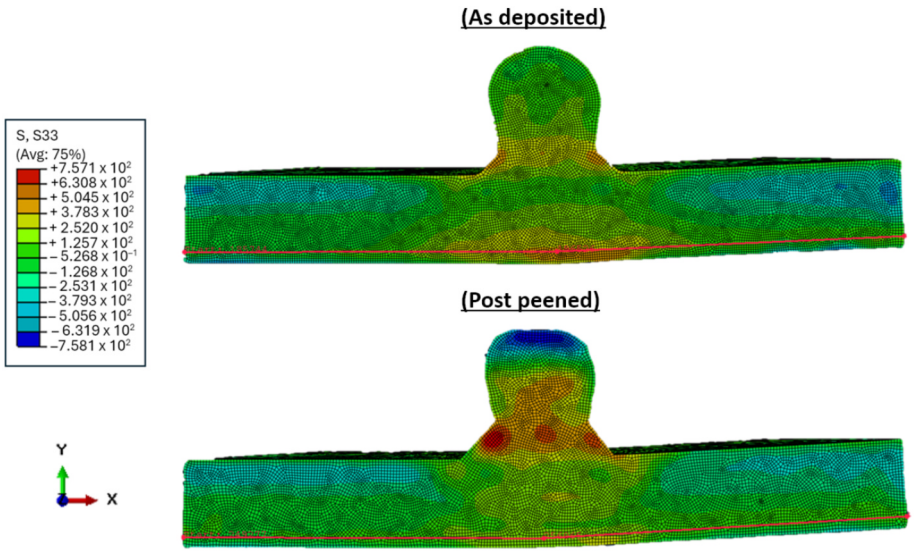


Fig. 17. FE analysis models for both the as-deposited and post-peened samples with back-calculated RS (in MPa) using CM.

spaced along each side in the longitudinal direction.

Despite the presence of distortion, it is unlikely to affect the ToF measurements, as the deformation resembles angular shrinkage rather than buckling, which would impact surface flatness. This phenomenon has been discussed in previous studies, such as the work by Sattari-Far and Javadi [32], who found that distortion in welded pipes did not significantly affect RS measurements when comparing FE model predictions with experimental data.

The resulting CM FE models, along with the back-calculated RS distributions, are shown in Fig. 17.

5.3. X-ray diffraction

Fig. 18 shows the XRD RS measurements of the as-deposited Ti-6Al-4V WAAM sample. Only an as-deposited sample was chosen for this measurement method to provide further validation of the RS measurements of the PAURS measurements. The results presented only consider the longitudinal stress measurements, as this is the main direction in which tensile RS occurs and where it is highest, so is the area mainly considered for RS measurements. As previously described, measurements were taken at 15 different points on the bottom of the sample, which are shown in the results.

As shown in the results, the RS distribution from the XRD measurements of the as-deposited WAAM Ti-6Al-4V sample aligns well with the expected stress zones. The RS reaches a peak of approximately 190 MPa at the centre of the sample wall, as expected. Within the HAZ, particularly between −10 and 5 mm, the RS remains relatively high, ranging from around 80 MPa to 90 MPa.

Further from the HAZ, particularly between 15 to 25 mm, the RS values are significantly lower, ranging from approximately ~ -60 MPa to ~ -30 MPa, and remain below zero in these outer regions.

Overall, the RS distribution follows the expected profile and appears relatively symmetrical. However, similar to CM results, a slight asymmetry is present. This is attributed to the same distortion on one side of the as-deposited WAAM sample, as previously discussed.

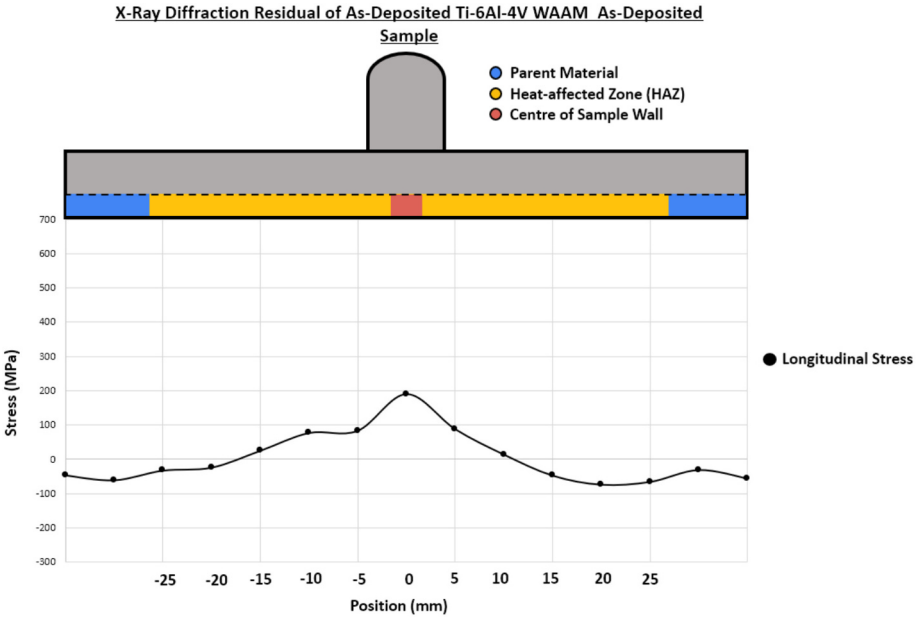


Fig. 18. XRD RS measurements of the as-deposited WAAM Ti-6Al-4V sample.

5.4. PAURS

5.4.1. Wedge angle testing

The optimal wedge angle for ultrasonic RS measurements in Ti-6Al-4V was determined following the Snell's law-based approach described in previous work by Walker et al [10]. A set of acrylic wedges with angles near the first critical angle for LCR waves in titanium alloys, ranging from 22.2° to 23.2°, was tested. The angle requiring the least gain adjustment for accurate ToF measurements was selected, resulting in an optimal wedge angle of 22.7° for the PAURS setup.

5.4.2. Full matrix capture

The improved accuracy of PAURS primarily comes from using FMC, an advanced phased-array technique where each element transmits while all others receive, creating a complete transmit–receive matrix. FMC enhances data redundancy, enables outlier removal, and improves RS accuracy by generating 64 LCR paths [40].

5.4.3. Signal-to-noise ratio (SNR)

Although the PAURS setup is capable of generating 64 LCR wave paths, not all of these paths are usable. In WAAM samples, the strength of LCR signals can be affected due to various factors, including noise and interference from other ultrasonic wave modes, such as shear waves. To assess the quality of the LCR signals and determine their reliability, it is essential to calculate the Signal-to-Noise Ratio (SNR).

SNR was calculated for each of the 64 LCR paths in the as-deposited Ti-6Al-4V sample across three distinct regions: the parent material, the −25 mm scan line, and the centre of the sample wall (0 mm), as shown in Fig. 12. To ensure consistency and repeatability in the SNR evaluation, a standardised methodology was developed. This methodology was applied across all sample locations and LCR paths and is shown in Fig. 19.

As part of the methodology, an example signal from the Ti-6Al-4V parent material is used to demonstrate how the SNR is calculated. The time window between 7 μs and 9 μs was selected for all acoustic paths and samples, as this region consistently contains both the LCR signal and the peak noise, allowing for a good comparison.

To calculate the SNR, the amplitude of the LCR signal was first identified within this window. Then, the peak noise amplitude was determined by selecting four distinct noise peaks within the same region. The average of these four peaks was used to reduce variability and improve consistency in the measurement. These values were then applied to the standard SNR formula to compute the final SNR for each path.

It is important to consider the results across all acoustic paths and regions to fully understand the signal quality. These results are shown in Fig. 20.

The calculated SNR values are generally consistent across all acoustic paths and regions, ranging from approximately 0 dB to 53 dB, with a few significant anomalies. Among the three regions, the parent material shows the most consistent SNR and the lowest overall noise levels. The −25 mm scan line, located at the edge of the measurement area, shows higher SNR values than the HAZ region, which is expected due to reduced interference.

Across all positions, the SNR follows a repeating pattern. It tends to remain stable or gradually increase, peaking at every eighth path before decreasing again. This pattern is observed consistently from path 8 through to path 64 and is likely related to the way ultrasound propagates using FMC, as shown in Fig. 9. As the acoustic paths progress from the first transmitter through each set of eight receivers, the SNR appears to increase across the receiver group before resetting with the next transmitter.

Interestingly, the SNR results are not entirely consistent with expectations. The parent material, which should exhibit minimal variation, shows more fluctuation than anticipated. Notable spikes occur at path 30 with 51 dB and path 33 with 53 dB, followed by a return to the previous SNR range. In contrast, the WAAM sample shows slightly more stable SNR values than expected. This improved consistency may be due to the WAAM measurements being retaken later using an updated method to enhance RS accuracy, which was not carried out for the parent material.

The SNR results in Fig. 20 indicate a clear correlation between signal quality and measurement reliability. Paths with SNR above ~ 40 dB, such as those observed in the parent material, consistently produced stable RS profiles without unrealistic peaks. In contrast, paths within the HAZ, where SNR was typically below 10 dB, were more prone to interpolation errors and generated extreme outliers during initial PAURS calculations. This supports the expectation that higher SNR improves zero-crossing detection and reduces timing uncertainty. Therefore, SNR serves as a practical criterion for identifying unreliable

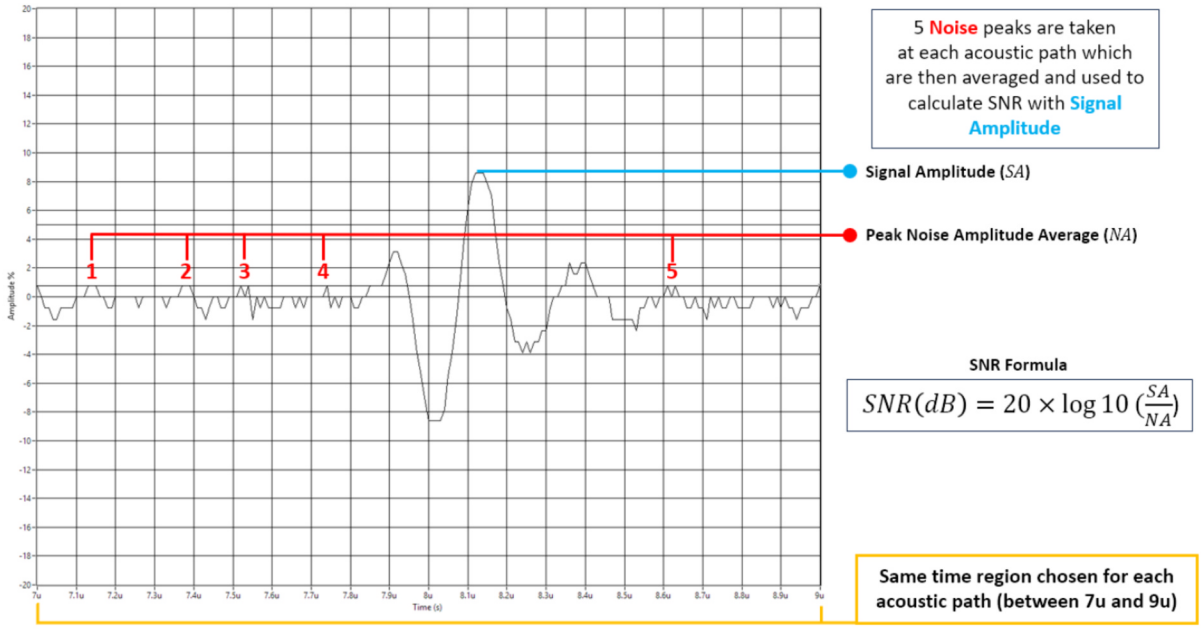


Fig. 19. SNR calculation methodology and formula.

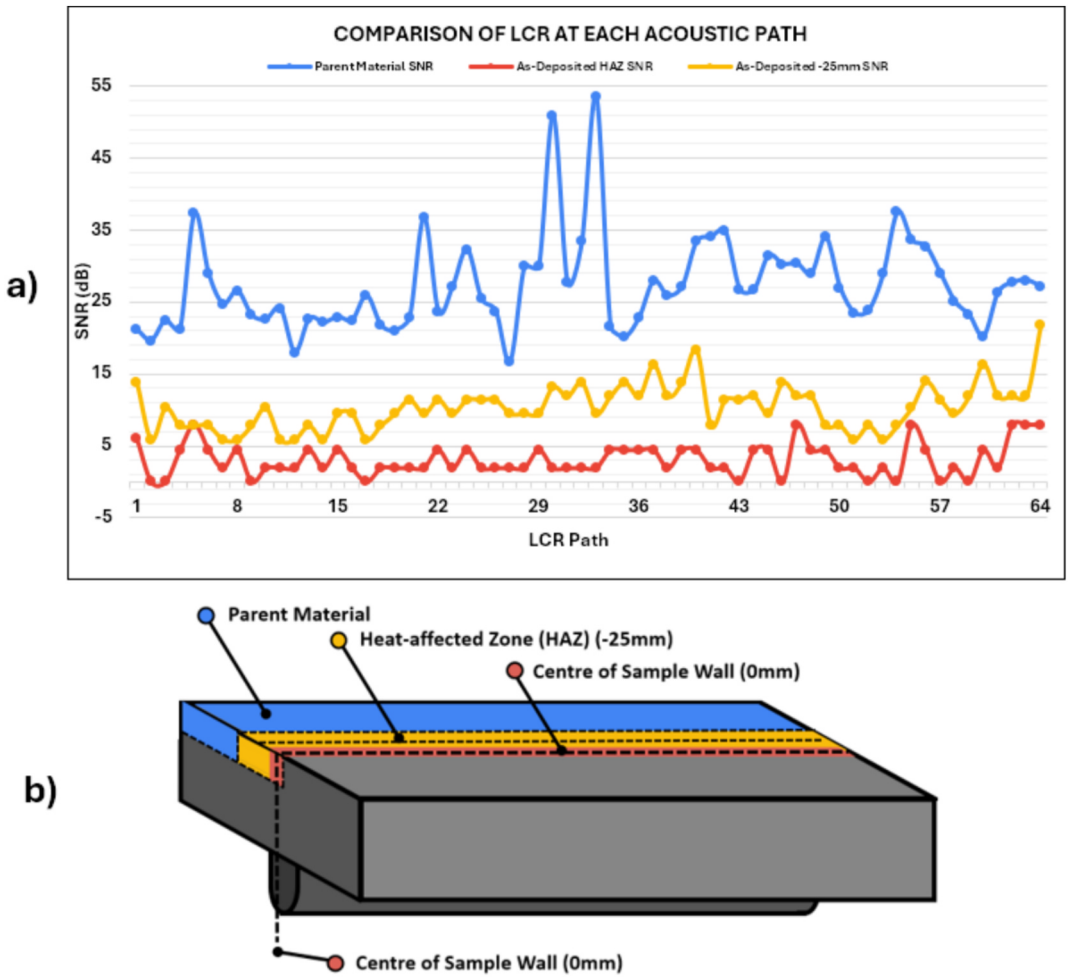


Fig. 20. (a) SNR results across regions; (b) Sample positions.

paths and guiding outlier removal during FMC-based averaging.

5.4.4. *Acoustoelastic constant*

The results from this experiment were previously discussed in the study by Walker et al. [10]. During the experiment, stress increments were applied through both loading and unloading cycles, allowing acoustoelastic constant measurements to be obtained separately for each mode. Since the PAURS setup uses two eight-element arrays, results can be presented individually for each element. This means that a total of 16 sets of data are produced when using the direct approach, with eight sets of data for loading and eight for unloading.

Figs. 21 and 22 show the acoustoelastic constant results for both loading and unloading, respectively. Each set of data corresponds to a specific array element, with data points collected using FMC. For example, "Element 3″ refers to the ToF measurement between transmitter element 3 and receiver element 3.

The vertical axis of each graph represents the value of Exdt/t0, where the slope of the graph corresponds to the acoustoelastic constant. This

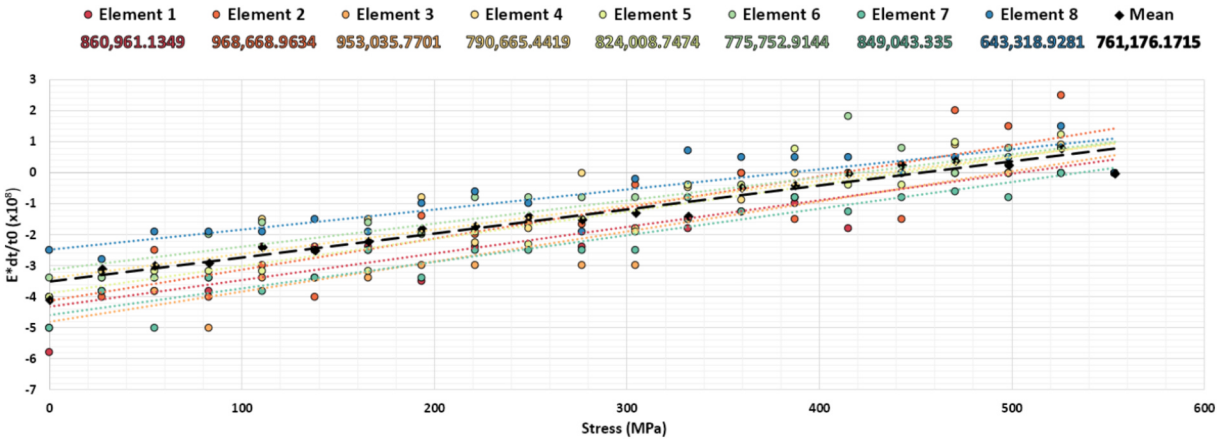


Fig. 21. Acoustoelastic constant graph during loading.

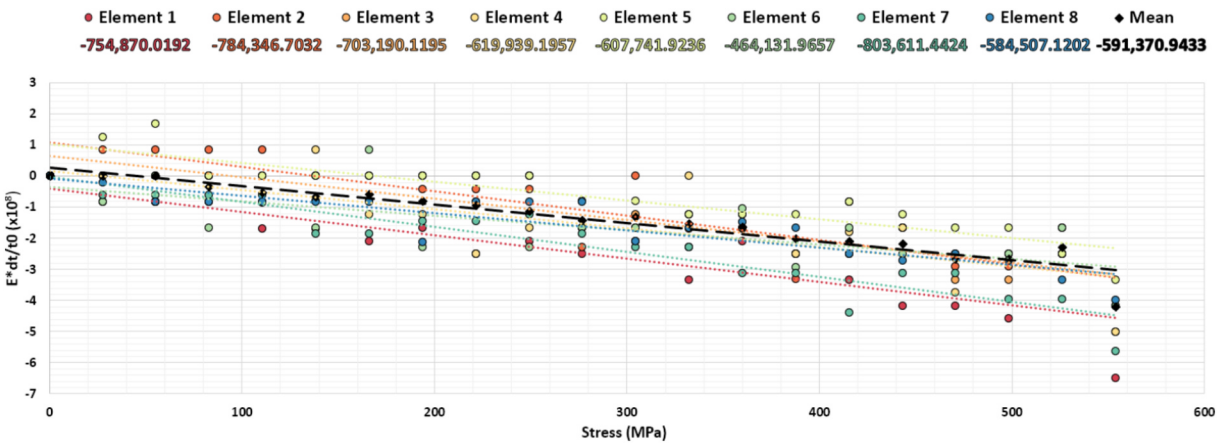


Fig. 22. Acoustoelastic constant graph during unloading.

constant is calculated by plotting the known stress applied by the tensile testing machine against the effective Young's modulus of the material. The acoustoelastic constant is then extracted from the best-fit line through the data points, which is shown in red on each graph.

As expected, the loading graph shows an upward trend, with increasing stress resulting in higher values of Exdt/t0, while the unloading graph displays the opposite pattern. However, a few outliers deviate from this trend. For instance, in the loading data, Element 6 shows an unexpected spike just after 400 MPa, followed by a gradual decrease. A similar anomaly appears in the unloading data at approximately 150 MPa for both Elements 4 and 6. Additionally, there are instances where the Exdt/t0 value remains constant over a wide stress range, despite a significant increase in applied stress.

These irregularities may be attributed to known sources of error discussed in previous studies by Javadi et al. [9] and Walker et al. [10], such as triggering issues or inconsistencies in the tensile testing machine. However, the impact of these errors is largely mitigated in the PAURS setup. Unlike traditional single-element ultrasonic methods, which rely on a single measurement and are more vulnerable to such anomalies, PAURS collects hundreds of data points across multiple paths. These are averaged to produce more reliable acoustoelastic constant measurements, allowing for greater confidence in the results and easier identification of outliers.

The Exdt/t0 values for each element are shown in Tables 2 and 3 for loading and unloading, respectively.

5.4.5. Final PAURS measurements

The PAURS measurement method was applied to both the as-deposited and inter-pass peened WAAM Ti-6Al-4V samples. This allowed for a direct comparison between the two conditions, as well as with the CM results, providing insight into both the effectiveness of inter-pass peening and the suitability of phased array ultrasound for RS evaluation in WAAM components. All RS measurements are measured with a penetration depth of 1.2 mm, as discussed previously from the macrographs. This depth is below the heat-affected zone, so it is unaffected by WAAM thermal cycles and retains a uniform microstructure across the section.

Table 2
Loading acoustoelastic constant results.

Element	Exdt/t0
1	860,961.1349
2	968,668.9634
3	953,035.7701
4	790,665.4419
5	824,008.7474
6	775,752.9144
7	849,043.335
8	643,318.9281
Mean	761,176.1715

Table 3
Unloading acoustoelastic constant results.

Element	Exdt/t0
1	−754,870.0192
2	−784,346.7032
3	−703,190.1195
4	−619,939.1957
5	−607,641.9236
6	−464,131.9657
7	−803,611.4424
8	−584,507.1202
Mean	−591,370.9433

The initial results from these measurements are presented in Figs. 23 and 24 for as-deposited and inter-pass peened samples, respectively. These were obtained using the path difference method illustrated in Fig. 19, where adjacent ToF values are subtracted to reduce the influence of couplant thickness on the RS measurements. Therefore, 56 acoustic paths are shown due to subtracting adjacent ToF to mitigate the effect of couplant thickness on the RS measurements.

The initial RS measurements obtained using the PAURS method show several noticeable outliers that significantly affect the overall results for both the as-deposited and inter-pass peened WAAM Ti-6Al-4V samples. In both datasets, the red line represents the mean RS across all acoustic paths. However, in many cases, individual RS measurements deviate substantially from this mean, indicating the presence of outliers.

For the as-deposited sample, several acoustic paths between 0 mm and 5 mm show RS values as high as approximately 6000 MPa, which is far above the expected range. Additionally, between −10 mm and 10 mm, some paths report RS values between −6000 MPa and −8000 MPa. Outside the HAZ, path 56 shows a clear anomaly between 10 mm and 25 mm, where RS spikes to around 2000 MPa.

Similarly, the inter-pass peened sample contains outliers, with several paths showing peak RS values between 4000 MPa and 6000 MPa. In the same central region between −10 mm and 10 mm, some paths report extremely low RS values, ranging from −6000 MPa to −10,000 MPa.

These outliers must be removed to ensure accurate RS measurements. One advantage of the PAURS method is that it generates 56 acoustic path measurements, allowing for a mean RS to be calculated and compared against individual paths. This makes it easier to identify and isolate outliers.

Figs. 25 and 26 present the standard deviation results for the as-deposited and inter-pass peened samples, respectively. Although

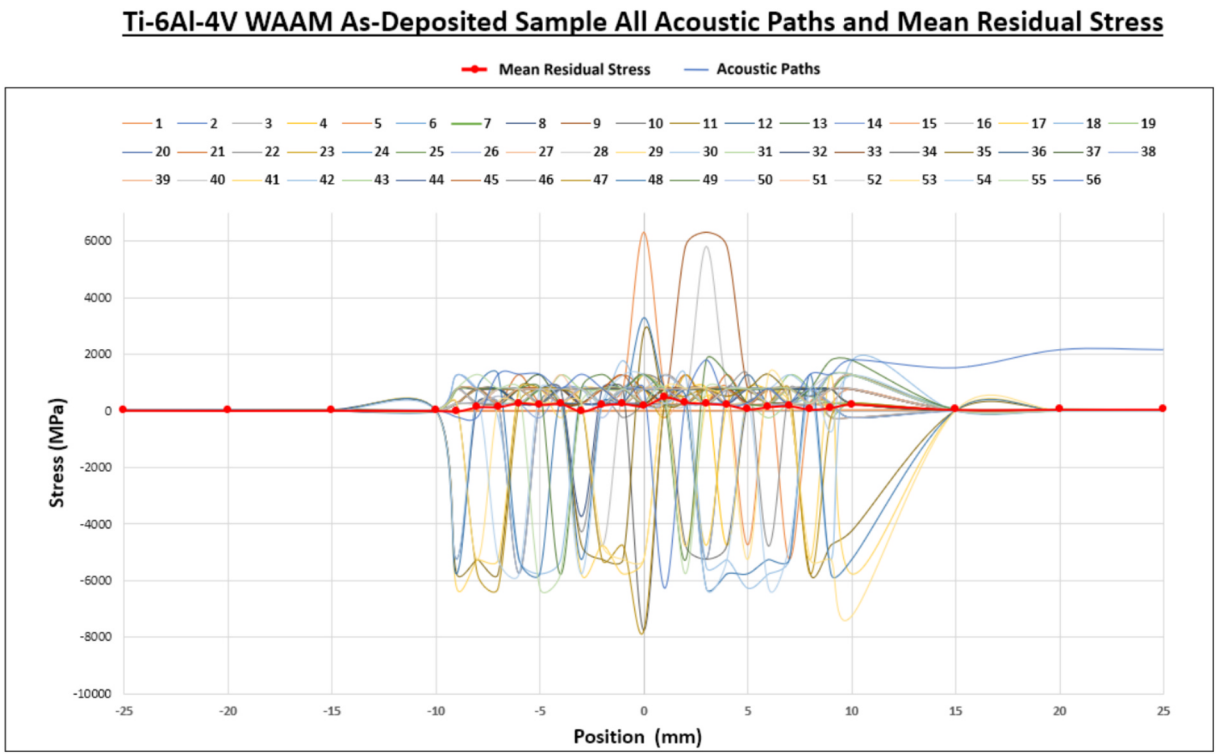


Fig. 23. As-Deposited initial RS measurements.

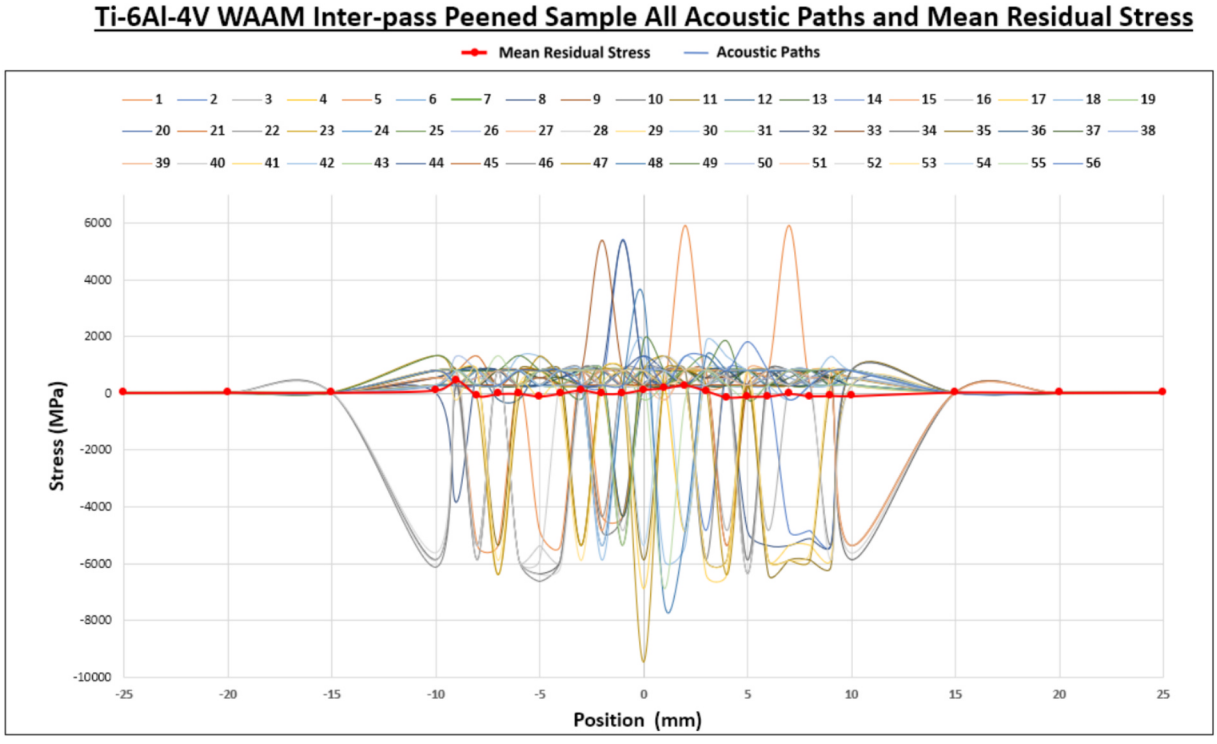


Fig. 24. Inter-pass Peened initial RS measurements.

standard deviation was calculated for all 56 paths, a set of 8 paths from each sample is shown to demonstrate how this method helps identify and remove outliers.

Outliers were identified using the standard deviation method, with a threshold of 100 MPa. This value was chosen based on two factors:

(i) Material yield strength: Ti-6Al-4V typically exhibits a yield strength of 850–950 MPa [41]. Even under extreme conditions, RS exceeding ~ 120 % of the yield strength of 1100 MPa is highly unlikely. Therefore, any calculated RS values in the range of several thousand MPa are physically unrealistic and indicative of measurement or interpolation errors.

(ii) Statistical consistency and prior studies: Previous ultrasonic RS

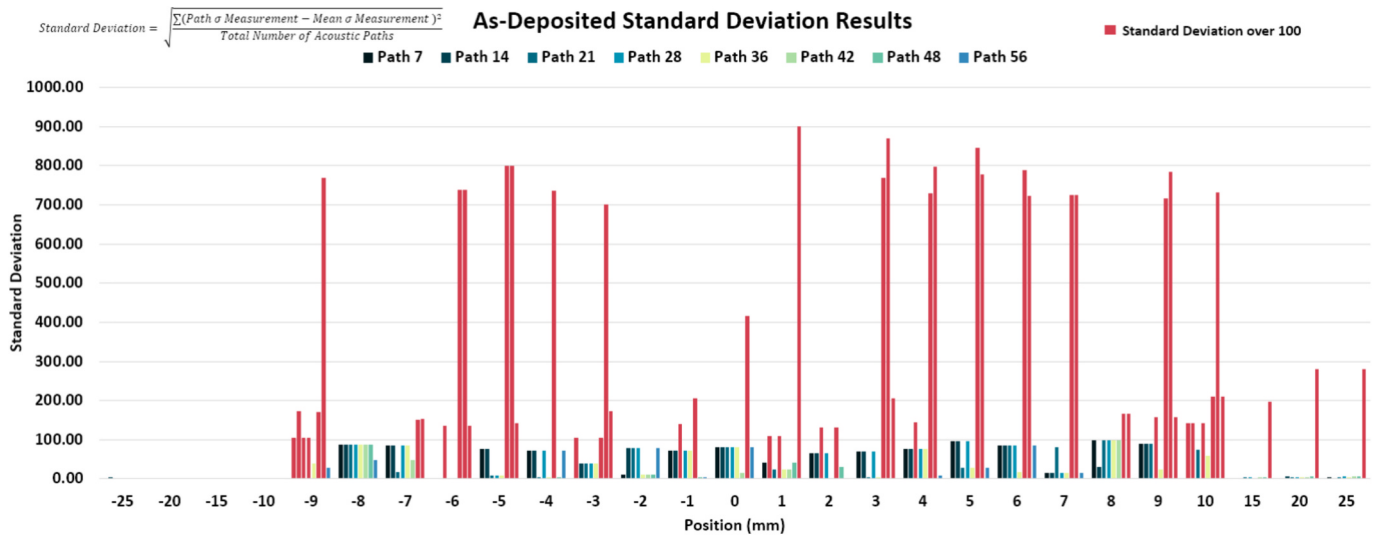


Fig. 25. As-deposited Standard Deviation results.

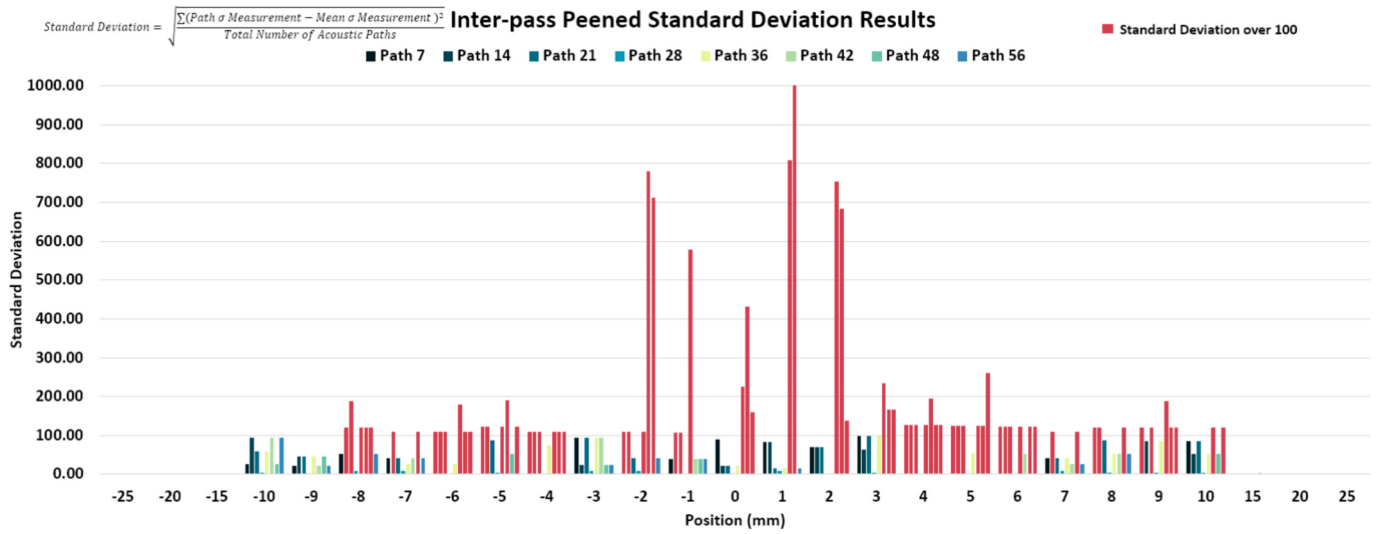


Fig. 26. Inter-pass peened Standard Deviation results.

studies [11,42,43] have shown that outlier rejection based on statistical dispersion, such as standard deviation, is effective for mitigating noise and coupling inconsistencies. A 100 MPa threshold is small relative to the material's yield strength yet large enough to accommodate naturally occurring variability in ultrasonic measurements, ensuring that genuine stress variations are preserved while extreme anomalies are removed.

A trend was observed in both samples where paths between 42 and 56 showed significantly more deviation from the mean. This may be due to poor contact between the transducer elements and the sample surface, particularly at the ends of the arrays. Elements 6 to 8 may therefore produce less reliable data. However, because PAURS averages results across all paths, the impact of these inaccuracies can be mitigated.

A trend was observed in both samples where paths between 42 and 56 showed significantly more deviation from the mean. These paths correspond to combinations involving the outer elements of the phased array (particularly Elements 6 to 8), which are more affected by poor coupling and uneven contact with the sample surface. This issue is common in array setups because the ends of the transducer often experience less consistent pressure compared to the elements at the centre. While a single-element transducer can also suffer from coupling inconsistencies, the impact is more pronounced in phased arrays due to the larger number of elements and the reliance on multiple transmit–receive combinations. However, PAURS mitigates this by averaging results across 56 acoustic paths, reducing the influence of any single unreliable path on the final RS measurement.

After removing the identified outliers, the final as-deposited and inter-pass peened RS measurements were produced and are shown in Figs. 27 and 28, respectively. As illustrated, the individual acoustic paths now align much more closely with the mean RS values, and the RS measurements fall within the expected range for both the as-deposited and inter-pass peened samples. A clear reduction in RS is observed in the inter-pass peened sample, confirming the effectiveness of the peening process in reducing tensile stress within the WAAM Ti-6Al-4V structure.

It is important to note that RS values up to 1300 MPa were not considered outliers in this study. This decision was based on the yield strength of Ti-6Al-4V, which typically ranges between 850 MPa and 950 MPa depending on processing conditions [44]. Assuming a threshold of 120 % of yield strength, values up to approximately 1140 MPa [45] could still be considered in regions of high RS. The 1300 MPa measurements, whilst much higher than the mean, were consistent with surrounding data and did not exhibit the behaviour typical of true

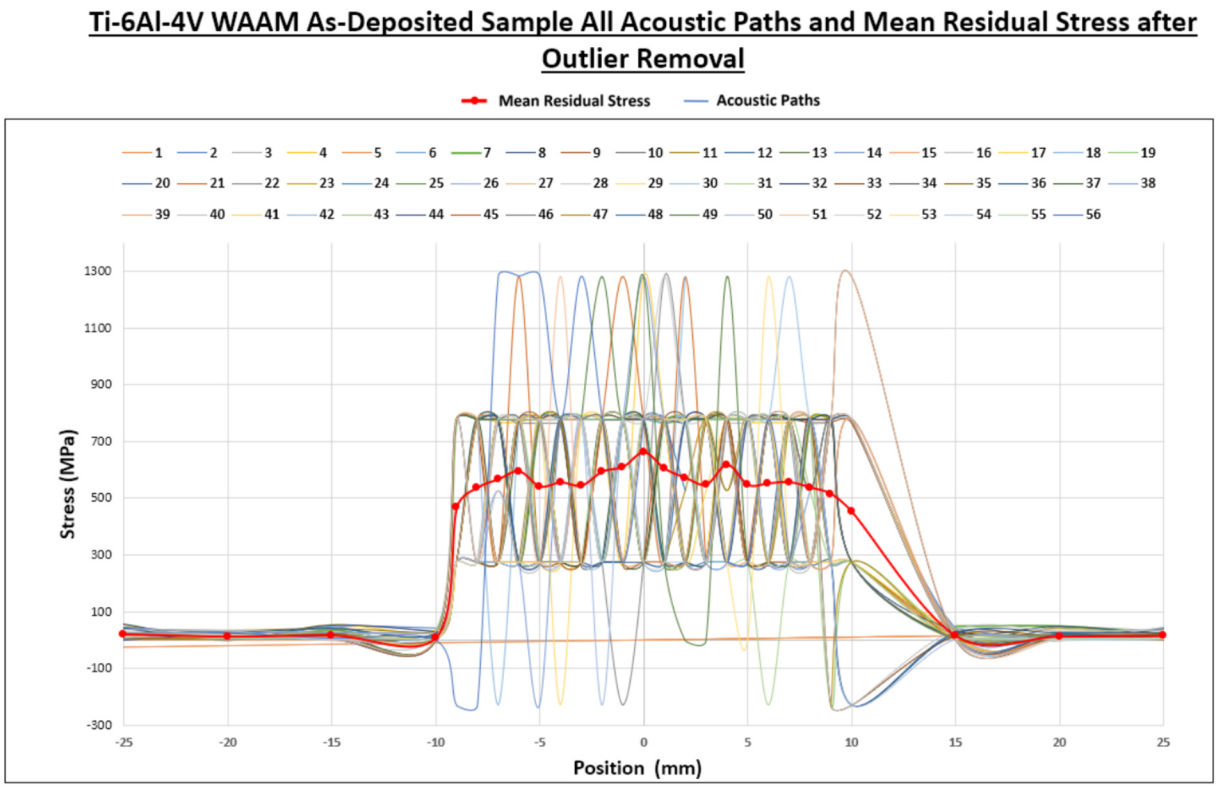


Fig. 27. As-deposited RS measurements after outlier removal.

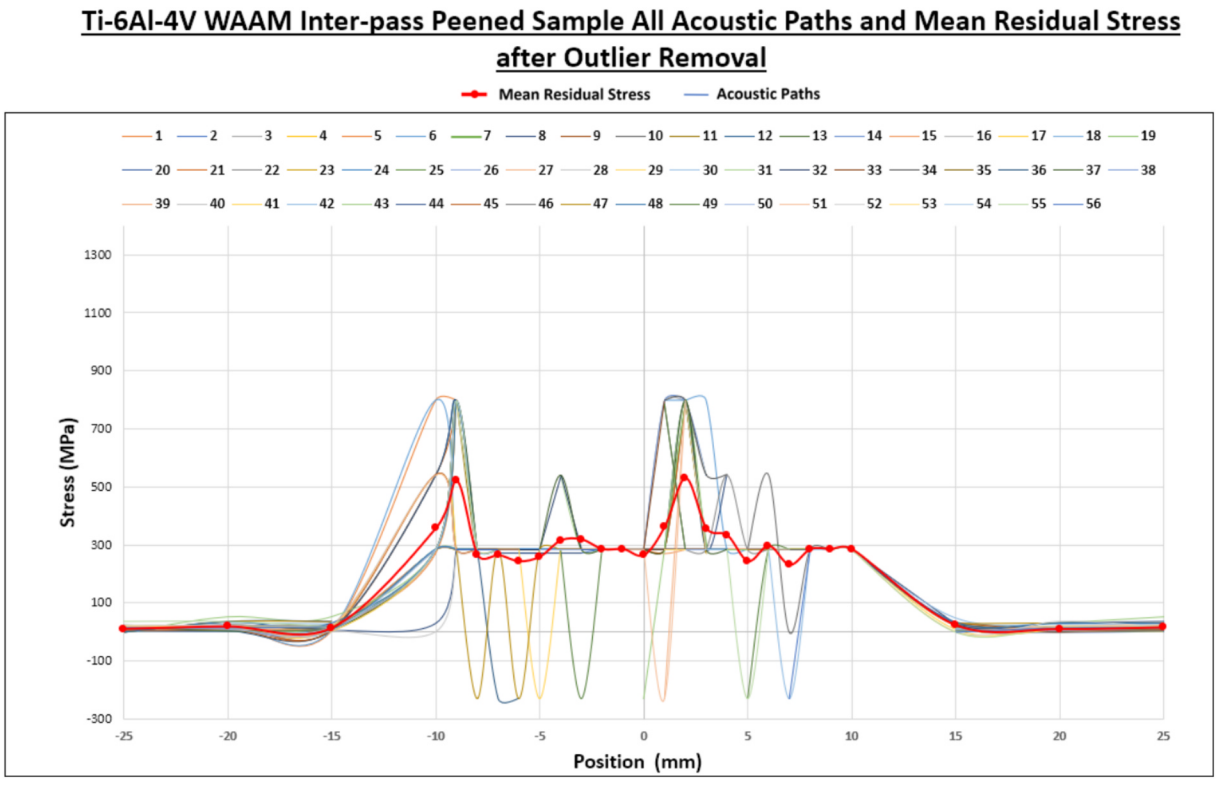


Fig. 28. Inter-pass peened RS measurements after outlier removal.

outliers, such as the extreme values exceeding 6000 MPa.

The comparison between the mean RS values before and after outlier removal is shown further in Fig. 29, clearly demonstrating improved accuracy in both the as-deposited and inter-pass peened samples. The RS measurements after outlier removal align more closely with the expected values for WAAM Ti-6Al-4V components. One of the most

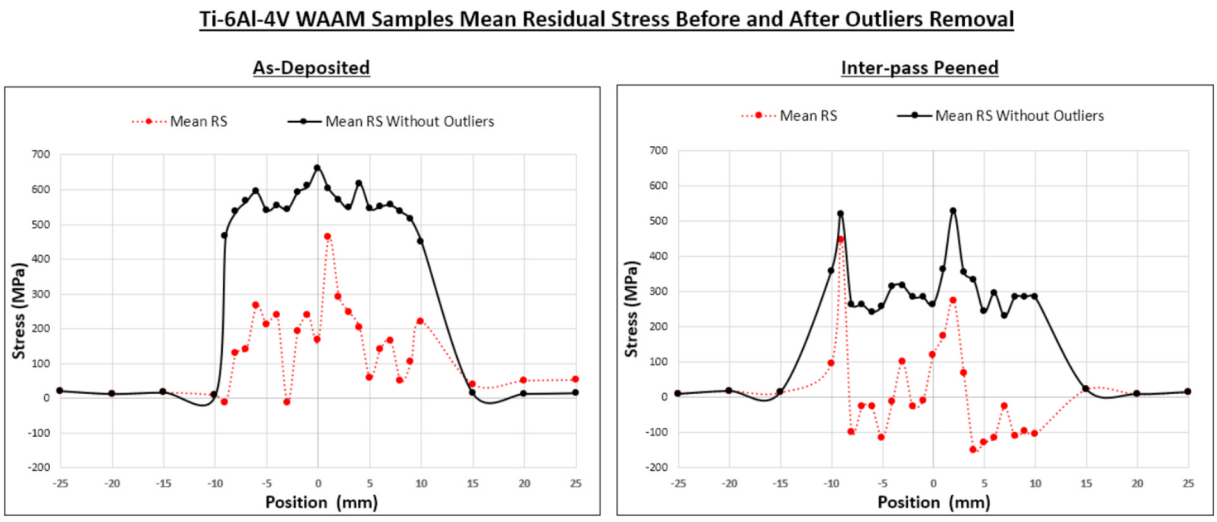


Fig. 29. Comparison of Mean RS before and after outlier removal.

notable observations is the higher concentration of outliers within the HAZ, particularly between −10 mm and 10 mm in both samples. Outside the HAZ, the removal of outliers has had a lesser effect, except for the region beyond 15 mm in the as-deposited sample. This corresponds to previously identified errors in path 56, which showed abnormal RS values between 10 mm and 25 mm. Removing this path led to a clear improvement in that area.

In the as-deposited sample, the overall RS distribution remains largely unchanged in shape after outlier removal. However, the RS values are significantly higher, with the peak increasing from ~ 480 MPa to ~ 660 MPa. The removal of outliers also greatly reduced fluctuations within the HAZ, resulting in a smoother and more natural RS curve between −10 mm and 10 mm. The peak RS now occurs at the centre of the sample wall (0 mm), as expected. These fluctuations were previously caused by extremely low RS values, with some acoustic paths measuring as low as −6000 MPa.

For the inter-pass peened sample, the overall RS shape also remains mostly consistent, but the RS values increase across the sample after outlier removal. This is due to similar issues as in the as-deposited sample, where several acoustic paths showed unrealistically low RS values between −6000 MPa and −10,000 MPa. Interestingly, the location of the peak RS shifts. Initially, the peak RS was observed at −10 mm with a value of ~ 450 MPa. After outlier removal, this increases slightly to ~ 520 MPa. However, a more significant change occurs at 2 mm, where the RS increases from ~ 280 MPa to ~ 530 MPa, indicating that this region was heavily affected by outliers. Outside the HAZ, the RS remains close to 0 MPa on both sides of the sample.

Fig. 30 presents the final mean RS measurements for both the as-deposited and inter-pass peened WAAM Ti-6Al-4V samples. Alongside the RS data, a schematic of a WAAM sample is included to illustrate the specific regions where measurements were taken, as previously shown in Fig. 12.

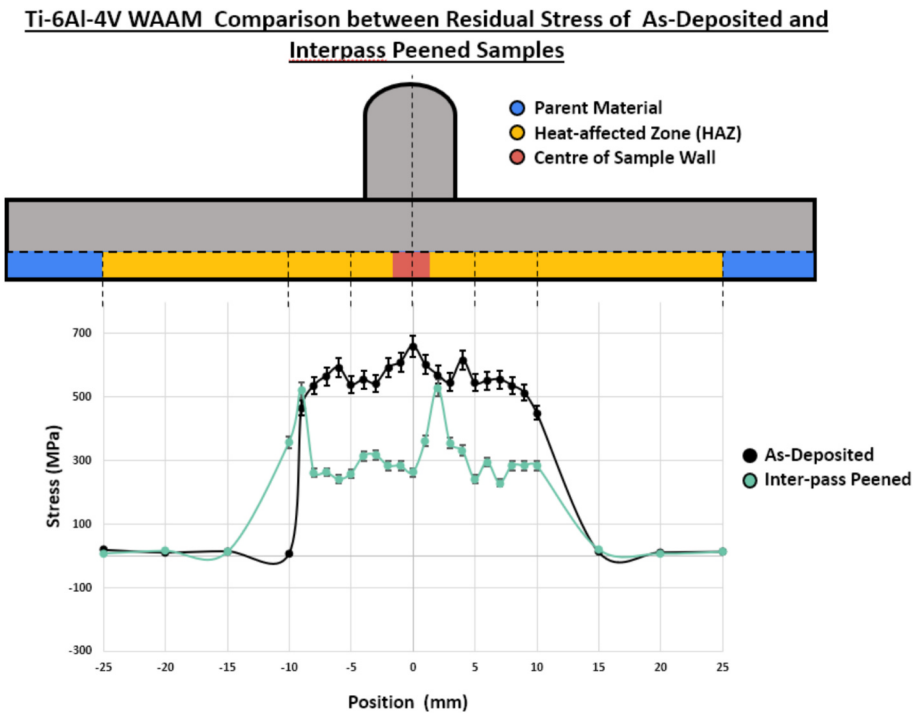


Fig. 30. Final Mean RS measurements for as-deposited and inter-pass peened samples.

Fig. 30 shows that both the as-deposited and inter-pass peened samples show the expected RS distribution, with higher RS values concentrated near the centre of the sample, between −10 mm and 10 mm. This region corresponds to the area most affected by heat during the WAAM process. Outside of this central zone, RS values drop significantly, with both samples measuring approximately 0 MPa, as expected.

The overall RS profile of the inter-pass peened sample closely resembles that of the as-deposited sample, but with noticeably lower RS values in the central region. Excluding the peak RS values, the average RS between −10 mm and 10 mm decreases from ~ 500–600 MPa in the as-deposited sample to around 250–300 MPa in the inter-pass peened sample. This reduction demonstrates the effectiveness of inter-pass peening in lowering overall RS.

However, two significant RS spikes remain in the inter-pass peened sample at −10 mm, −9 mm, and 2 mm, where RS values reach ~ 350 MPa, 520 MPa, and 530 MPa, respectively. Notably, the RS at −10 mm and −9 mm is higher in the inter-pass peened sample than in the as-deposited one, increasing from 0 MPa to 360 MPa at −10 mm and from 480 MPa to 520 MPa at −9 mm. While this may suggest that peening increased RS at these points, it is more likely that the process redistributed stress within the HAZ. The reduction in RS across the rest of the HAZ may have concentrated stress at these specific locations. Additionally, inter-pass peening may have replaced harmful tensile stress with beneficial compressive stress, improving the overall structural integrity of the sample.

Overall, the comparison between both samples and their respective scan areas confirms that PAURS provides accurate RS measurements for WAAM Ti-6Al-4V. For example, the peak RS of approximately 680 MPa occurs precisely at 0 mm, aligning with the centre of the sample wall where the highest thermal input is expected. The similarity in RS distribution between the two samples, along with the clear reduction in RS in the inter-pass peened sample, further supports the reliability of the PAURS method.

5.5. Comparison of PAURS, CM, and XRD results

Fig. 31 shows a comparison of RS results across multiple measurement methods and sample conditions. It includes CM results for both the as-deposited and post-peened samples, PAURS results for the as-deposited and inter-pass peened samples, and XRD results for the as-deposited sample.

Despite differences in measurement principles and data acquisition techniques, all three methods show strong qualitative agreement in RS distribution. In each case, the peak RS occurs at the centre of the sample wall (0 mm), where thermal input during WAAM is most concentrated in the HAZ, and RS decreases as it is measured further from the HAZ.

The PAURS results are notably smoother than those obtained using CM and show significantly less fluctuation, particularly in regions such as 0–5 mm and 45–60 mm, where CM shows notable instability. XRD results are similarly smooth, and PAURS further improves consistency using FMC, which enables anomaly detection and removal.

For the as-deposited Ti-6Al-4V samples, the PAURS method recorded the highest peak at ~ 680 MPa, followed by CM at around 410 MPa. XRD measured the lowest peak RS, with ~ 190 MPa.

The quantitative differences in peak RS values can be attributed to the inherent characteristics of each technique. PAURS measures near-surface stress over a depth of approximately 1–1.2 mm and uses ultrasonic velocity changes, which are highly sensitive to local stress variations [10]. The use of FMC and interpolation enhances resolution, allowing detection of sharper stress gradients and higher peak values [11]. In contrast, CM provides an averaged stress distribution across the entire cross-section after material removal, which tends to smooth out localised peaks [24]. XRD measures only the top few microns of the

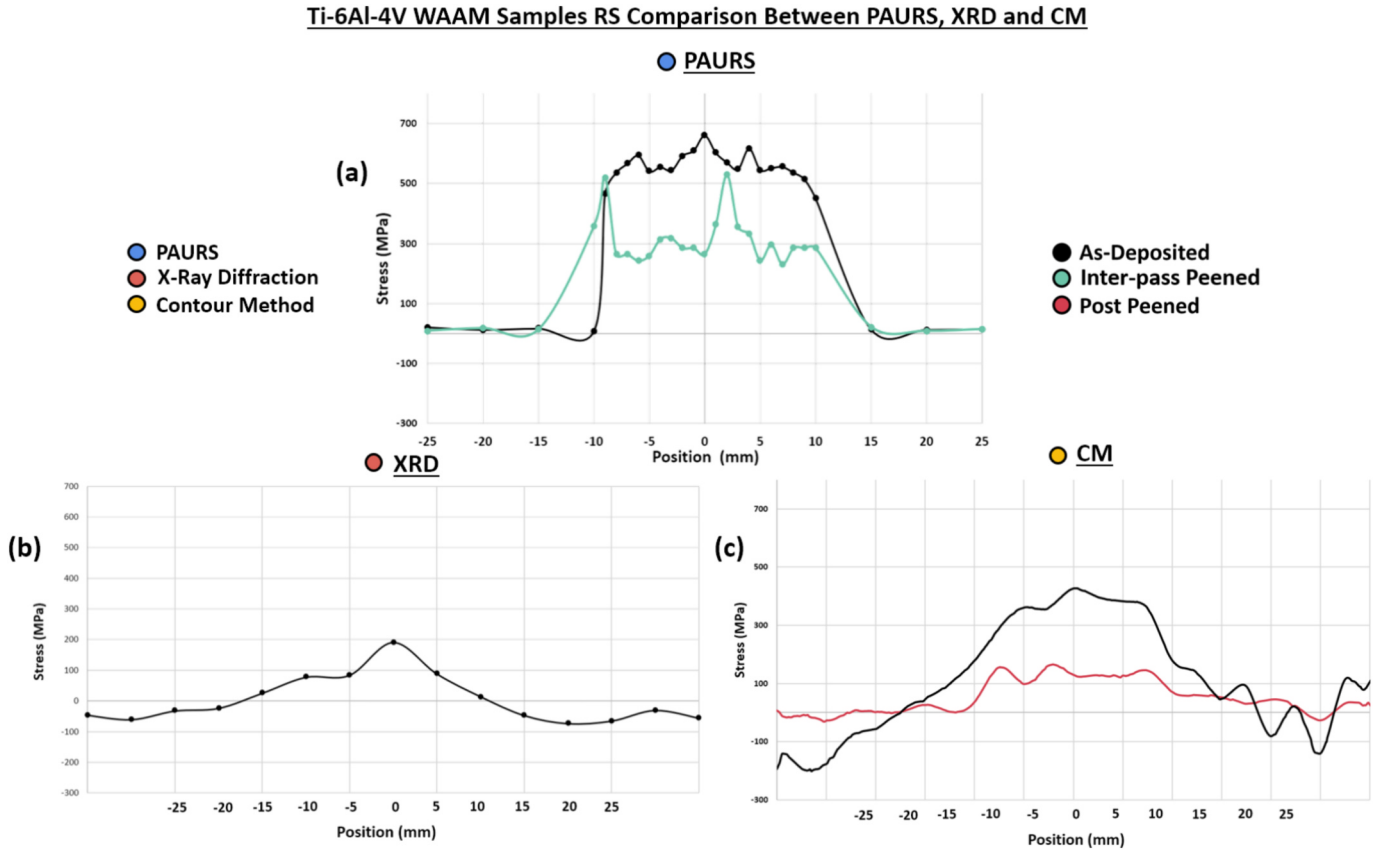


Fig. 31. (a) Final PAURS RS measurements, (b) XRD as-deposited RS, (c) CM RS for as-deposited and post-peened samples.

surface, where stress relaxation and microstructural effects can reduce tensile stress compared to subsurface regions [28]. Additionally, differences in spatial resolution, penetration depth, and data processing, such as FE reconstruction using CM against LCR path averaging using PAURS, contribute to these discrepancies [7]. These variations are consistent with prior comparative studies of RS measurement techniques and highlight the importance of considering method-specific sensitivities when interpreting RS data [3].

The very small penetration depth of XRD means that it is not the best to study the effect of peening on the peened surface directly. However, this was out of the scope of this paper, in which the bottom surface was studied, but the potential of using PAURS and XRD for RS measurement on the WAAM wall is in the vision of the work.

Both inter-pass peening (measured using PAURS) and post-peening (measured using CM) demonstrate clear effectiveness in reducing RS. PAURS shows a reduction of approximately 200–250 MPa in peak RS in the inter-pass peened sample compared to the as-deposited sample. Similarly, CM shows a reduction of around 300 MPa in the post-peened sample. Although the inter-pass peened sample shows a higher peak RS (~500 MPa) than the post-peened sample (~130 MPa), this difference is likely due to the measurement method rather than the peening process itself. The elevated values in PAURS may result from FMC-based anomaly removal, which enhances peak detection, and from the nature of inter-pass peening, which may redistribute stress and replace tensile RS with beneficial compressive RS.

Importantly, PAURS is the only method among the three with the potential for in-process RS measurement. As discussed by Javadi et al [9], this ability enables real-time evaluation of inter-pass peening effectiveness. Manufacturers can use PAURS to assess RS immediately after each deposition pass and determine whether additional peening is necessary, without waiting for post-process inspection. Moreover, PAURS can be used in-situ, meaning the sample does not need to be unclamped or transferred to another measurement setup. This is particularly advantageous for both inter-pass and post-process evaluation, as it avoids stress redistribution that may occur during handling. In contrast, while XRD is also non-destructive, it requires specialised facilities and is not suitable for in-process or in-situ applications. CM, although capable of providing full FE RS modelling, is destructive and requires the sample to be cut, making it unsuitable for iterative or real-time evaluation.

Based on these findings, PAURS demonstrates strong potential as a method for RS measurements in WAAM components. Although each investigated method offers unique advantages and limitations, PAURS stands out as the only method capable of in-process and in-situ RS measurement, making it particularly valuable for evaluating the effectiveness of inter-pass peening. Both PAURS and XRD are non-destructive, while CM is destructive but provides comprehensive RS measurements and modelling. The ability of PAURS to support real-time decision-making during manufacturing, combined with its adaptability and depth of measurement, makes it a highly effective tool for RS evaluation in WAAM Ti-6Al-4V components.

5.6. Limitations and extensions

While this study has demonstrated the capability of PAURS for RS evaluation, it also has several limitations, which highlight directions for future work. First, PAURS measurements were limited to the bottom surface of the WAAM samples. Due to the use of 5 MHz arrays with limited penetration depth, the current setup cannot directly access RS within the WAAM wall. This constraint will be addressed in future developments by integrating phased array probes into a roller-probe configuration developed for in-process defect-detection of the wall [46]. Such an approach represents a key justification for PAURS, as it is the only current method with the potential to evolve into a practical in-process RS measurement tool [11].

A second limitation arises from coupling effects. Although techniques such as path-difference analysis and FMC averaging were used to mitigate couplant thickness variation and edge-element inconsistencies (see Section 4.4.7), these factors remain sources of error and point to the need for further refinement in transducer design and coupling methods.

The influence of microstructure on both RS evaluation and ultrasonic propagation was also not directly characterised in this work. Variations in grain morphology, such as columnar-equiaxed transitions, and anisotropy effects could affect CM accuracy and ultrasonic velocity [17,31]. Prior work has shown that ultrasonics can detect gross changes in anisotropy and grain aspect ratio [9,11], suggesting that combining PAURS with complementary microstructural characterisation would provide a more comprehensive framework for process control and structural integrity in WAAM components.

Finally, while both inter-pass and post-peening strategies demonstrated measurable reductions in RS, a direct comparison of their effectiveness is restricted by the use of different measurement techniques, with PAURS for inter-pass peening and CM for post-peening. This introduces variability due to differences in penetration depth and spatial resolution [10]. Nevertheless, qualitative trends remain consistent, and both methods significantly reduce tensile RS in the heat-affected zone compared to the as-deposited condition [8].

From a practical standpoint, inter-pass peening offers the advantage of being integrated into the WAAM process, enabling real-time mitigation of stress accumulation without removing the component from the setup. This reduces the risk of distortion during handling and opens the possibility for in-process monitoring when combined with PAURS [11]. However, its effectiveness may be influenced by process parameters such as peening frequency and energy per blow, and it requires careful synchronisation with deposition to avoid surface defects [12].

Conversely, post-peening provides greater flexibility in applying higher-intensity treatments after the component has cooled, which can lead to more uniform stress redistribution [12]. It is less constrained by deposition timing but introduces additional manufacturing steps and handling, which may allow partial stress relaxation before treatment [47]. Furthermore, post-peening cannot prevent distortion during the build, whereas inter-pass peening can mitigate these effects progressively [48].

In summary, inter-pass peening is advantageous for large, complex WAAM components where in-process stress control is critical, while post-peening remains valuable for achieving deeper and more uniform stress redistribution when process integration is less feasible [48]. Future work should include applying the same measurement method to both conditions or combining PAURS and CM on identical samples to enable a fully quantitative comparison [10].

6. Conclusions

This study investigated the use of PAURS measurements on WAAM Ti-6Al-4V samples in both as-deposited and inter-pass peened conditions. The results were compared with CM and XRD measurements to evaluate the feasibility of PAURS and the effectiveness of inter-pass peening as a RS mitigation strategy. The following conclusions were drawn:

PAURS proved to be a viable method for RS measurement in WAAM Ti-6Al-4V, demonstrating improved accuracy using FMC and 64 acoustic paths, which enabled outlier removal and enhanced result reliability.

PAURS and XRD as-deposited results displayed more stable results with significantly less fluctuations than the CM results. While PAURS and CM differed quantitatively, with PAURS showing RS peaks of ~ 500–650 MPa and CM showing ~ 400–450 MPa, they remained within a comparable range. XRD showed lower peak RS (~190 MPa) but followed a similar distribution.

Qualitatively, all three methods agreed, with PAURS offering the most stable results and significantly reduced fluctuation compared to CM, especially outside the HAZ.

Error-reduction techniques in PAURS, such as couplant thickness correction and FMC-based data averaging, contributed to more accurate and consistent RS measurements.

Inter-pass peening effectively reduced RS in WAAM Ti-6Al-4V. When comparing the PAURS-measured inter-pass peened sample with the CM-measured post-peened sample, both showed RS reductions in the HAZ—~250 MPa for inter-pass peening and ~ 300 MPa for post-peening. The differences in peak RS are likely due to the measurement methods rather than the peening processes themselves.

Based on the findings, PAURS is strongly recommended as a reliable RS measurement method for WAAM Ti-6Al-4V components. Additionally, inter-pass peening is validated as an effective RS mitigation technique, offering practical benefits during the manufacturing process.

7. Funding Statement

This research was funded by the EPSRC, NEWAM grant number (EP/R027218/1).

CRediT authorship contribution statement

Joseph Walker: Writing – review & editing, Writing – original draft, Visualization, Validation, Software, Methodology, Investigation, Formal analysis, Data curation, Conceptualization. **Brandon Mills:** Software, Investigation, Data curation. **Yashar Javadi:** Writing – review & editing, Writing – original draft, Supervision, Project administration, Funding acquisition, Formal analysis, Conceptualization, Resources. **Charles MacLeod:** Writing – review & editing, Software, Resources. **Yongle Sun:** Writing – review & editing, Writing – original draft, Resources, Data curation, Conceptualization. **Bilal Ahmad:** Writing – original draft, Resources, Data curation. **Stewart Williams:** Resources, Funding acquisition. **Jialuo Ding:** Resources, Data curation. **Saeed Tamimi:** Writing – original draft, Resources, Data curation, Investigation, Writing – review & editing.

Declaration of competing interest

The authors declare that they have no known competing financial interests or personal relationships that could have appeared to influence the work reported in this paper.

Acknowledgements

The authors would like to acknowledge the support of NEWAM (EPSRC grant EP/R027218/1) for the production of the samples.

Data availability

Data will be made available on request.

References

[1] Wu, B., Pan, Z., Ding, D., Cuiuri, D., Li, H., Xu, J., Norrish, J.: A review of the wire arc additive manufacturing of metals: properties, defects and quality improvement, 2018.
[2] A. Caballero, J. Ding, Y. Bandari, S. Williams, Oxidation of Ti-6Al-4V during Wire and Arc Additive Manufacture, 3D Print. Addit. Manuf. 6 (2019) 91–98, https://doi.org/10.1089/3dp.2017.0144.
[3] J.A. Francis, Measurement, modelling and mitigation of residual stress, Mater. Sci. Technol. 32 (2016) 1409–1410, https://doi.org/10.1080/02670836.2016.1232476.
[4] Champaigne, J.: Shot Peening Overview. (2001).
[5] F. Martina, M.J. Roy, B.A. Szost, S. Terzi, P.A. Colegrove, S.W. Williams, P. J. Withers, J. Meyer, M. Hofmann, Residual stress of as-deposited and rolled wire+arc additive manufacturing Ti–6Al–4V components, Mater. Sci. Technol. 32 (2016) 1439–1448, https://doi.org/10.1080/02670836.2016.1142704.
[6] A. Tognan, L. Laurenti, E. Salvati, Contour method with uncertainty quantification: a robust and optimised framework via gaussian process regression, Exp. Mech. 62 (2022) 1305–1317, https://doi.org/10.1007/s11340-022-00842-w.
[7] N.S. Rossini, M. Dassisti, K.Y. Benyounis, A.G. Olabi, Methods of measuring residual stresses in components, Mater. Des. 35 (2012) 572–588, https://doi.org/10.1016/j.matdes.2011.08.022.
[8] B. Ahmad, X. Zhang, H. Guo, M.E. Fitzpatrick, L.M.S.C. Neto, S. Williams, Influence of deposition strategies on residual stress in wire + arc additive manufactured titanium Ti-6Al-4V, Metals (basel) 12 (2022) 253, https://doi.org/10.3390/met12020253.
[9] Javadi, Y., Hutchison, A., Zimermann, R., Singh, J., Mohseni, E., Rahimi, S., Mehnen, J., Macleod, C., Pierce, G., Tant, K., Gachagan, A.: Feasibility study of residual stress measurement using phased array ultrasonic method Feasibility study of residual stress measurement using phased array ultrasonic method FEASIBILITY STUDY OF RESIDUAL STRESS MEASUREMENT USING PHASED ARRAY ULTRASONIC METHOD. (2022).
[10] J. Walker, B. Mills, Y. Javadi, C. MacLeod, Y. Sun, P.K. Taraphdar, B. Ahmad, S. Gurumurthy, J. Ding, F. Sillars, Study of residual stress using phased array ultrasonics in Ti-6AL-4V Wire-Arc additively manufactured components, Sensors 24 (2024) 6372, https://doi.org/10.3390/s24196372.
[11] B. Mills, J. Walker, Y. Javadi, C.N. MacLeod, H. Alipooramirabad, M. Reid, A. Paradowska, Residual stress analysis in robotically welded plates using phased array ultrasonics with validation through neutron diffraction and hole-drilling methods, Int. J. Press. Vessel. Pip. 216 (2025) 105518, https://doi.org/10.1016/j.ijpvp.2025.105518.
[12] L. Neto, S. Williams, A.E. Davis, J.R. Kennedy, Effect of machine hammer peening conditions on β grain refinement of additively manufactured Ti-6Al-4V, Metals (Basel) 13 (2023) 1888, https://doi.org/10.3390/met13111888.
[13] G. Xian, J. Pan, J. Lee, N. Kang, Weakening the anisotropic property and refining prior-β grains via hammer peening treatment during wire arc additively manufacturing of Ti-6Al-4V, Metals (Basel) 14 (2024) 1261, https://doi.org/10.3390/met14111261.
[14] J.R. Hönnige, A.E. Davis, A. Ho, J.R. Kennedy, L. Neto, P. Prangnell, S. Williams, The effectiveness of grain refinement by machine hammer peening in high deposition rate wire-arc AM Ti-6Al-4V, Metall. Mater. Trans. A 51 (2020) 3692–3703, https://doi.org/10.1007/s11661-020-05781-6.
[15] Neto, L., Williams, S., Ding, J., Hönnige, J., Martina, F.: Mechanical Properties Enhancement of Additive Manufactured Ti-6Al-4V by Machine Hammer Peening. Presented at the (2020).
[16] F.D. Gurmesa, H.G. Lemu, Literature review on thermomechanical modelling and analysis of residual stress effects in wire arc additive manufacturing, Metals (Basel) 13 (2023) 526, https://doi.org/10.3390/met13030526.
[17] P.J. Withers, H.K.D.H. Bhadeshia, Residual stress. Part 2 – Nature and origins, Mater. Sci. Technol. 17 (2001) 366–375, https://doi.org/10.1179/026708301101510087.
[18] P.J. Withers, Residual stress and its role in failure, Rep. Prog. Phys. 70 (2007) 2211–2264, https://doi.org/10.1088/0034-4885/70/12/R04.
[19] Fry, A.T.: A review of residual stress measurement methods A guide to technique selection. (2001).
[20] N. Bastola, M.P. Jahan, N. Rangasamy, C.S. Rakurty, A review of the residual stress generation in metal additive manufacturing: analysis of cause, measurement, effects, and prevention, Micromachines (Basel) 14 (2023) 1480, https://doi.org/10.3390/mi14071480.
[21] G.E. Totten, M.A.H. Howes, Inoue Tatsuo, Handbook of residual stress and deformation of steel, ASM International (2002).
[22] M.B. Prime, The two-way relationship between residual stress and fatigue/fracture. In: Conference Proceedings of the Society for Experimental Mechanics Series. Springer New York LLC, 2018, pp. 19–23.
[23] H.F. Bueckner, The propagation of cracks and the energy of elastic deformation, J. Fluids Eng. 80 (1958) 1225–1229, https://doi.org/10.1115/1.4012657.
[24] Prime, M.B., Hill, M.R.: Residual Stress Mapping in Welds Using the Contour Method, 2002.
[25] Prevey, P.S.: X-RAY DIFFRACTION RESIDUAL STRESS TECHNIQUES, 1986.
[26] Stacey, A., Macgillivary, H.J., Webster, G.A., Webster, P.J., Ziebeck, K.R.A.: MEASUREMENT OF RESIDUAL STRESSES BY NEUTRON DIFFRACTION, 1985.
[27] M.D. Olson, A.T. DeWald, M.B. Prime, M.R. Hill, Estimation of uncertainty for contour method residual stress measurements, Exp. Mech. 55 (2015) 577–585, https://doi.org/10.1007/s11340-014-9971-2.
[28] Q. Luo, S. Yang, Uncertainty of the X-ray Diffraction (XRD) sin2 ψ Technique in measuring Residual Stresses of Physical Vapor Deposition (PVD) Hard Coatings, Coatings 7 (2017) 128, https://doi.org/10.3390/coatings7080128.
[29] Chan, S.Y., Pooja, C., Dennise, T.A., Keegan, L.: Evaluation of Measurement Uncertainty for Residual Stress Measurements using X-Ray Diffraction. (2017).
[30] Javadi, Y., Hutchison, A., Zimermann, R., Singh, J., Mohseni, E., Rahimi, S., Mehnen, J., Macleod, C., Pierce, G., Tant, K., Gachagan, A.: Feasibility study of residual stress measurement using phased array ultrasonic method Feasibility study of residual stress measurement using phased array ultrasonic method FEASIBILITY STUDY OF RESIDUAL STRESS MEASUREMENT USING PHASED ARRAY ULTRASONIC METHOD. (2022).
[31] Bray, D.E.: Current directions of Ultrasonic Stress Measurement Techniques.
[32] I. Sattari-Far, Y. Javadi, Influence of welding sequence on welding distortions in pipes, Int. J. Press. Vessel. Pip. 85 (2008) 265–274, https://doi.org/10.1016/j.ijpvp.2007.07.003.
[33] Ramuhalli, P., Good, M.S., Diaz, A.A., Anderson, M.T., Watson, B.E., Peters, T.J., Dixit, M., Bond, L.J.: Ultrasonic Characterization of Cast Austenitic Stainless Steel Microstructure: Discrimination between Equiaxed- and Columnar-Grain Material ? An Interim Study. , Richland, WA (United States) (2009).

[34] R.J. Lavarello, G. Ghoshal, M.L. Oelze, On the estimation of backscatter coefficients using single-element focused transducers, J. Acoust. Soc. Am. 129 (2011) 2903–2911, https://doi.org/10.1121/1.3557036.
[35] S.I. Rokhlin, G. Sha, J. Li, A.L. Pilchak, Inversion methodology for ultrasonic characterization of polycrystals with clusters of preferentially oriented grains, Ultrasonics 115 (2021) 106433, https://doi.org/10.1016/j.ultras.2021.106433.
[36] Y. Liu, A. Van Pamel, P.B. Nagy, P. Cawley, Investigation of ultrasonic backscatter using three-dimensional finite element simulations, J. Acoust. Soc. Am. 145 (2019) 1584–1595, https://doi.org/10.1121/1.5094783.
[37] J. Zhang, Y. Song, X. Li, C. Zhong, Comparison of experimental measurements of material grain size using ultrasound, J. Nondestr. Eval. 39 (2020) 30, https://doi.org/10.1007/s10921-020-00675-4.
[38] J.J. Lin, Y.H. Lv, Y.X. Liu, B.S. Xu, Z. Sun, Z.G. Li, Y.X. Wu, Microstructural evolution and mechanical properties of Ti-6Al-4V wall deposited by pulsed plasma arc additive manufacturing, Mater. Des. 102 (2016) 30–40, https://doi.org/10.1016/j.matdes.2016.04.018.
[39] C. Hicks, S. Tamimi, G. Sivaswamy, M. Pimentel, S. McKegney, S. Fitzpatrick, Hybrid manufacturing approach for landing gear applications: WAAM Ti–6Al–4V on forged Ti–5Al–5Mo–5V–3Cr, J. Mater. Res. Technol. 30 (2024) 6596–6608, https://doi.org/10.1016/j.jmrt.2024.05.088.
[40] C. Holmes, B.W. Drinkwater, P.D. Wilcox, Post-processing of the full matrix of ultrasonic transmit–receive array data for non-destructive evaluation, NDT & E International. 38 (2005) 701–711, https://doi.org/10.1016/j.ndteint.2005.04.002.
[41] R. Sun, L. Li, Y. Zhu, W. Guo, P. Peng, B. Cong, J. Sun, Z. Che, B. Li, C. Guo, L. Liu, Microstructure, residual stress and tensile properties control of wire-arc additive manufactured 2319 aluminum alloy with laser shock peening, J. Alloys Compd. 747 (2018) 255–265, https://doi.org/10.1016/j.jallcom.2018.02.353.
[42] Y. Javadi, A. Hutchison, R. Zimermann, J. Singh, E. Mohseni, S. Rahimi, J. Mehnen, C. Macleod, G. Pierce, K. Tant, A. Gachagan, Feasibility study of residual stress measurement using phased array ultrasonic method Feasibility study of residual stress measurement using phased array ultrasonic method FEASIBILITY STUDY OF RESIDUAL STRESS MEASUREMENT USING PHASED ARRAY ULTRASONIC METHOD, 2022.
[43] D.E. Bray, W. Tang, Subsurface stress evaluation in steel plates and bars using the LCR ultrasonic wave, Nucl. Eng. Des. 207 (2001) 231–240, https://doi.org/10.1016/S0029-5493(01)00334-X.
[44] J. Sun, Y. Pan, Y. Liu, F. Kuang, R. Lu, X. Lu, Strength–ductility synergy strategy of Ti6Al4V alloy fabricated by metal injection molding, Int. J. Miner. Metall. Mater. 32 (2025) 1641–1654, https://doi.org/10.1007/s12613-024-3023-4.
[45] H. Shao, L. Cai, D. Shan, K. Wang, L. Li, G. Zhang, Y. Zhao, Microstructure and high strength–ductility synergy of Ti–6Al–4V alloy induced by joule heat treatment, J. Mater. Sci. 53 (2018) 16609–16617, https://doi.org/10.1007/s10853-018-2794-2.
[46] R. Zimermann, E. Mohseni, M. Vasilev, C. Loukas, R.K.W. Vithanage, C.N. Macleod, D. Lines, Y. Javadi, M.P. Espirindio E Silva, S. Fitzpatrick, S. Halavage, S. Mckegney, S.G. Pierce, S. Williams, J. Ding, Collaborative robotic wire + arc additive manufacture and sensor-enabled in-process ultrasonic non-destructive evaluation, Sensors 22 (2022) 4203, https://doi.org/10.3390/s22114203.
[47] S.W. Williams, F. Martina, A.C. Addison, J. Ding, G. Pardal, P. Colegrove, Wire + Arc Additive Manufacturing, Mater. Sci. Technol. 32 (2016) 641–647, https://doi.org/10.1179/1743284715Y.0000000073.
[48] S. Srivastava, R.K. Garg, V.S. Sharma, A. Sachdeva, Measurement and mitigation of residual stress in wire-arc additive manufacturing: a review of macro-scale continuum modelling approach, Arch. Comput. Meth. Eng. 28 (2021) 3491–3515, https://doi.org/10.1007/s11831-020-09511-4.



https://dspace.org/

Inter-pass peening for residual stress control in additive manufacturing: validation using ultrasonic, X-ray and contour method

Walker, Joseph; Mills, Brandon; Javadi, Yashar; MacLeod, Charles; Sun, Yongle ...

2025-12
Elsevier
https://doi.org/10.1016/j.matdes.2025.115247
Walker J, Mills B, Javadi Y, et al., (2025) Inter-pass peening for residual stress control in additive manufacturing: validation using ultrasonic, X-ray and contour method. Materials & Design, Volume 260, December 2025, Article number 115247

Downloaded from a DSpace repository. https://dspace.org/